NAVAL POSTGRADUATE SCHOOL

MONTEREY, CALIFORNIA

THESIS

INTEGRATION OF ADAPTIVE OPTICS INTO HIGH ENERGY LASER MODELING AND SIMULATION

by

Donald Puent

June 2017

Thesis Advisor: Keith Cohn
Co-Advisor: Joseph Blau

THIS PAGE INTENTIONALLY LEFT BLANK

REPORT DOCUMENTATION PAGE

Form Approved OMB No. 0704–0188

1. AGENCY USE ONLY *(Leave Blank)*	2. REPORT DATE	3. REPORT TYPE AND DATES COVERED
	June 2017	Master's Thesis (December 2016 to June 2017)

4. TITLE AND SUBTITLE

INTEGRATION OF ADAPTIVE OPTICS INTO HIGH ENERGY LASER MODELING AND SIMULATION

5. FUNDING NUMBERS

6. AUTHOR(S)

Donald Puent

7. PERFORMING ORGANIZATION NAME(S) AND ADDRESS(ES)

Naval Postgraduate School
Monterey, CA 93943

8. PERFORMING ORGANIZATION REPORT NUMBER

9. SPONSORING / MONITORING AGENCY NAME(S) AND ADDRESS(ES)

N/A

10. SPONSORING / MONITORING AGENCY REPORT NUMBER

11. SUPPLEMENTARY NOTES

The views expressed in this document are those of the author and do not reflect the official policy or position of the Department of Defense or the U.S. Government. IRB Protocol Number: NA.

12a. DISTRIBUTION / AVAILABILITY STATEMENT

Approved for public release. Distribution is unlimited.

12b. DISTRIBUTION CODE

13. ABSTRACT *(maximum 200 words)*

We investigate the corrective effect of adaptive optics (AO) on High Energy Laser (HEL) beam propagation through atmospheric turbulence. The effect of adaptive optics systems was first integrated into a laser propagation scaling code, ANCHOR, that was developed within the Direct Energy (DE) research group at the Naval Postgraduate School (NPS). Using a host of plausible input parameters, we then compare the estimated target irradiance increase accomplished by various adaptive optics systems. In various cases, adaptive optics is shown to substantially increase the effective range of HELs.

14. SUBJECT TERMS

directed energy, lasers, adaptive optics

15. NUMBER OF PAGES 71

16. PRICE CODE

17. SECURITY CLASSIFICATION OF REPORT	18. SECURITY CLASSIFICATION OF THIS PAGE	19. SECURITY CLASSIFICATION OF ABSTRACT	20. LIMITATION OF ABSTRACT
Unclassified	Unclassified	Unclassified	UU

NSN 7540-01-280-5500

Standard Form 298 (Rev. 2–89)
Prescribed by ANSI Std. 239–18

THIS PAGE INTENTIONALLY LEFT BLANK

Approved for public release. Distribution is unlimited.

INTEGRATION OF ADAPTIVE OPTICS INTO HIGH ENERGY LASER MODELING AND SIMULATION

Donald Puent
Ensign, United States Navy
B.S., United States Naval Academy, 2016

Submitted in partial fulfillment of the
requirements for the degree of

MASTER OF SCIENCE IN PHYSICS

from the

NAVAL POSTGRADUATE SCHOOL
June 2017

Approved by: Keith Cohn
Thesis Advisor

Joseph Blau
Thesis Co-Advisor

Kevin B. Smith
Chair, Department of Physics

THIS PAGE INTENTIONALLY LEFT BLANK

Abstract

We investigate the corrective effect of adaptive optics on High Energy Laser beam propagation through atmospheric turbulence. The effect of adaptive optics systems was first integrated into a laser propagation scaling code, ANCHOR, that was developed within the Direct Energy research group at the Naval Postgraduate School. Using a host of plausible input parameters, we then compare the estimated time-averaged target irradiance increase accomplished by various adaptive optics systems. In various cases, adaptive optics is shown to substantially increase the effective range of HELs.

THIS PAGE INTENTIONALLY LEFT BLANK

Contents

List of Figures

List of Tables

THIS PAGE INTENTIONALLY LEFT BLANK

Acknowledgments

I would like to thank Professor Keith Cohn and Professor Joseph Blau for their tireless effort in helping me conduct my work and prepare my thesis. Their endless presence and consistent feedback helped me stay on track and turn this work into the best product it could have been.

THIS PAGE INTENTIONALLY LEFT BLANK

CHAPTER ONE

Introduction

The U.S. Navy is constantly predicting future threats and contemplating new weapon technologies to counter them. One of those technologies is directed-energy (DE) weapons. Conventional weapons rely on the kinetic energy of projectiles. High energy lasers (HELs), one type of directed-energy weapon, work in a fundamentally new way, using electromagnetic radiation to damage or destroy enemy assets.

High energy lasers offer several advantages over conventional weapons, including the delivery of energy at light speed, a low cost per shot, virtually unlimited magazines, ability to rapidly engage several targets, and ability to operate discreetly. Despite the many advantages, DE weapons also have some disadvantages to conventional weapons, including a high susceptibility to performance degradation in challenging atmospheric conditions.

The technology of adaptive optics (AO) has proven useful in mitigating the effects of the atmosphere on light beam propagation in the field of astronomy [1], where AO is often used to improve image resolution. Likewise, AO shows promise in improving HEL performance. To better understand how much adaptive optics can improve HEL performance and facilitate sound decision making on whether or not to integrate adaptive optics with HELs, we simulate the effect of adaptive optics on laser beam irradiance and compare that to cases without adaptive optics. Many simulations have been created that accomplish this by using numerical diffraction methods. Uniquely, we incorporate adaptive optics into a scaling law code to facilitate large parameter studies.

THIS PAGE INTENTIONALLY LEFT BLANK

CHAPTER TWO

Overview of Directed Energy

Directed-energy weapons include all weapons that project electromagnetic radiation. High energy lasers are one of the most promising DE weapons and have already undergone some field testing. All conventional lasers use the process of stimulated emission to emit a coherent light beam.

2.1 Laser Technology Overview

The process of stimulated emission was first introduced in 1917 by Albert Einstein, but it would take until 1960 before the first laser was built by Theodore H. Maiman. Stimulated emission describes the process of a photon of light perturbing an excited electron, causing the electron to drop to a lower energy state and emit a coherent photon of the same frequency, polarization, and direction as the initial perturbing photon. For this process to amplify light, electrons must be energized into the excited state, creating population inversion. The material containing the excited electrons is called the gain medium and can be made from a variety of materials. A fundamental component of lasers is the optical cavity, which is the arrangement of mirrors that surrounds the gain medium and provides the feedback loop for stimulated emission to occur [2].

Laser designs have used several methods to achieve population inversion. Chemical lasers use chemical reactions while gas lasers typical use an electric current or optical pumping to excite gases. In weapons research, a common chemical laser is the deuterium fluoride laser, which creates fluorine atoms through combustion and combines deuterium and helium atoms with the fluorine atoms to create a stable population inversion. A common gas laser is the CO_2 laser, which achieves population inversion through burning a hydrocarbon and expanding the hot gas through nozzles. CO_2 lasers are used commercially in welding, drilling, and cutting [2].

Perhaps the most common designs in use today are solid state lasers (SSLs), which use solid state materials as the gain medium. Because the applications for solid state lasers are

so broad and numerous, the technology has matured rapidly over the past few decades. The ubiquity of conventional solid state lasers make them the most ready asset for near-term implementation of DE weapons on the battlefield. Fiber lasers are SSLs that use optical fibers as the gain medium, making them more rugged and efficient than previously developed SSLs. Slab lasers are a particular form of SSLs that use slabs for the gain medium, generally defined as large aspect ratio rectangular cross-section materials. Slab lasers offer a potential technological advantage over traditional rod lasers in their power-scalability [3].

A free electron laser (FEL) uses a relativistic electron beam from a particle accelerator as the gain medium. The electrons oscillate between a series of alternating permanent magnets, emitting light in the process [4]. The emitted light is captured inside of a resonator cavity that is similar to the mirror cavity of a conventional laser. Notably, the FEL does not require the use of a fixed gain medium with its associated heating and distortion issues, so FELs have the potential to be scaled to high output power. Additionally, FELs can be tuned to specific wavelengths and produce high quality light beams [4].

2.2 Advantages and Disadvantages of Directed-Energy Weapons

Laser weapons are fundamentally different than conventional weapons. As such, there are applications for which laser weapons are superior to conventional weapons and others for which conventional weapons are better. The delivery of energy through electromagnetic radiation, as opposed to the kinetic energy delivered by massive projectiles in conventional weapons, results in precise and fast payload delivery, permitting the engagement of quickly maneuvering targets. The variable power output of lasers also allow for a graduated response, enabling variations of damage that can result in "soft" or "hard" kills. Laser weapons are also desirable for their relatively low cost per shot and effectively infinite magazines [2].

Despite these advantages, directed-energy weapons do have some drawbacks. They are large and expensive to build. The propagation of laser light is highly dependent on atmospheric conditions and also requires a line-of-sight to the target. Moreover, a finite dwell time is required to disable or destroy targets; harder targets lead to dwell times of many seconds in some cases [5].

2.3 Brief History of Directed-Energy Weapons Development

The first conference on military applications of lasers occurred in 1963, three years after the first laser was created [6]. Since then, the U.S. military has invested in various project beginning with Project DELTA (CO_2 gas dynamic laser), Navy Advanced Chemical Laser, Army Mobile Tactical Unit (CO_2 electric discharge laser), and the Airborne Laser Lab (CO_2 gas dynamic laser) throughout the 1970s. From 1980-2000s, the Navy developed the MIRACL laser, a deuterium fluoride (DF) chemical laser that was the first megawatt class laser in the U.S. [7]. MIRACL successfully completed over 150 tests including shooting down missiles and drones [2, 6]. Perhaps the most well-known DE project was the hydrogen fluoride (HF) chemical Space-Based Laser in the 1980s, which was never completed [8]. The chemical oxygen iodine (COIL) Airborne Laser (ABL) was a U.S. Air Force project that began in 1996 and successfully destroyed a ballistic missile in 2010 before the project was canceled in 2014 [9]. The Tactical High Energy Laser (THEL) was a partnership between Israel and the U.S. Army from 1996-2005 that used a DF sub-megawatt laser and successfully shot down 28 Katyusha artillery rockets and 5 artillery shells over the course of the project [10]. U.S. Army Project ZEUS began in 1996, which uses a solid state laser of power ~10 kW to destroy land mines and Improved Explosive Devices (IEDs) and has been used successfully on the battlefield in Iraq and Afghanistan [11]. In 2002, the U.S. Air Force began the Advanced Tactical Laser as a follow on to the ABL that, again, used a COIL [2]. The Joint High Power Solid State Laser (JHPSSL) project ran from 2003-2010 and successfully combined 7 slab lasers to generate a laser of overall power ~100 kW and spawned follow on projects such as the Maritime Laser Demonstrator and the Robust Electric Laser Initiative [6]. Most recently, DE weapon projects include the High Energy Liquid Laser (2001-present), the Laser Weapons System (LaWS, 2010-present) shown in Figure 2.1 that has seen successful testing on the USS Ponce in the Arabian Gulf, and the Solid-State Laser Technical Maturation (SSL-TM) project, which has the goal of getting an HEL on a ship for testing and evaluation at sea by FY18 [6].

FIGURE 2.1 Picture of the U.S. Navy Laser Weapons System (LaWS) onboard the USS Ponce. Source: [12].

CHAPTER THREE

Atmospheric Propagation of High Energy Lasers

Light propagation through a vacuum is a well understood phenomena, but various fields of study require additional insight on how that propagation changes in the presence of an atmosphere. Several effects such as absorption, scattering, thermal blooming, and turbulence combine to diminish the irradiance and/or distort the beam as it propagates. Beam alteration is a function of wavelength and output power in addition to atmospheric conditions. Absorption, scattering, and turbulence are all linear effects, while thermal blooming is nonlinear; these effects combine at high output power to create an upper limit on the intensity of a light beam at the target. In the case of high energy lasers (HELs), the goal of characterizing these effects is to understand their physical limits in certain conditions and to develop a mechanism by which it is possible to mitigate them as much as possible in order to maximize the intensity of light on targets. We will look at these effects separately.

3.1 Absorption and Scattering

Absorption and scattering of photons by particles of gases and aerosols are crucial mechanisms that attenuate light. To understand these phenomena, we begin by examining what happens when photons interact with particles.

The analysis begins with a look at the probability that photons will collide with atmospheric particles and thereby be absorbed or scattered. Figure 3.1 shows the total effective area that is blocked by gas or aerosol particles in a volume V of the atmosphere. This effective area is given by the equation

$$A_{\text{eff}} = (N\sigma A)dz$$

where A_{eff} is the total area blocked by all the particles in V, N is the number density of particles, σ is the effective cross section area of a single particle, A is the cross section area of volume V, and dz is the thickness of volume V. To calculate the probability that photons

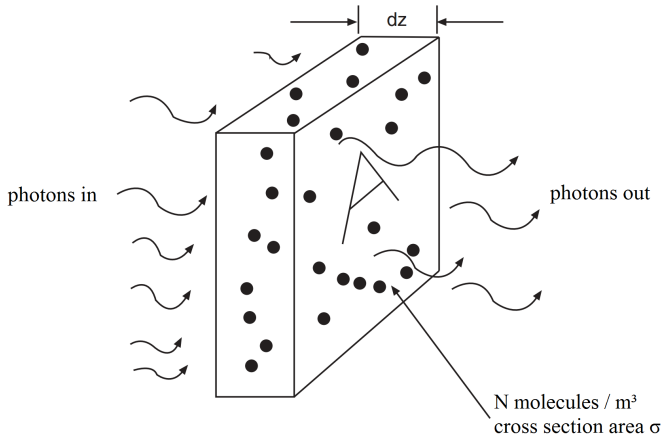

FIGURE 3.1 A volume of air, V, defined by cross section area, A, and width, dz, contains particles that absorb and scatter incoming light. Each of these processes contribute to the extinction of light. Adapted from [13].

traveling through volume V will be scattered or absorbed, we take the ratio A_{eff}/A, which yields

$$\text{probability of collision} = (N\sigma)dz.$$

It should also be noted that the cross-section σ depends on the particle as well as the type of interaction being considered.

The number of photons scattered or absorbed in the beam is proportional to the total number of photons multiplied by this probability. Since optical power P is proportional to the number of photons, the attenuated power dP becomes

$$\frac{dP}{P} = -(N\sigma)dz$$

where the minus sign indicates attenuation. The solution to this equation is the following:

$$P(z) = P(0)e^{-N\sigma z} \tag{3.1}$$

where $P(0)$ is the initial power and z is the coordinate along the beam path. This solution is known as *Beer's Law,* which simply states that light power attenuates exponentially as it propagates through the atmosphere. The attenuation or extinction coefficient is defined as

$$\epsilon = N\sigma.$$

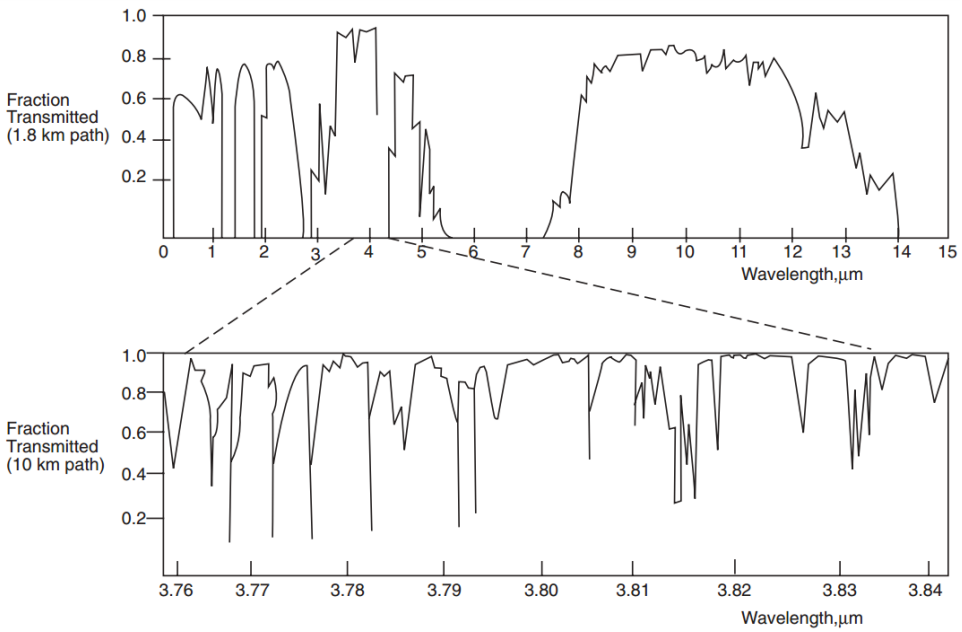

FIGURE 3.2 Plot of fractional transmittance ($T = P(z)/P(0)$) through the atmosphere as a function of wavelength. "Atmospheric windows" exist at high T values where the atmosphere is transparent. Even within atmospheric windows, there are bandwidths of high absorption. Source: [13].

This characterization of attenuation is not comprehensive, but is scalable for different types of gas and aerosol particles. The attenuation coefficient of each type of particle is largely independent of the coefficients of other types of particles present in the propagating medium, so the total coefficient is simply the sum of coefficients of each type of particle. Additionally, there are separate coefficients for absorption and scattering, expressed as

$$\epsilon = \alpha_m + \alpha_a + \beta_m + \beta_a$$

where α is the absorption contribution, β is the scattering contribution, and the subscripts m and a refer to gas molecules and aerosols, respectively. Each of these terms is a function of the wavelength since gas and aerosol particles will be optically transparent to some wavelengths and opaque at others.

Figure 3.2 illustrates the attenuation of light through the atmosphere over a broad range of wavelengths. The ranges of relative transparency are known as "propagation windows". The bottom chart in Figure 3.2 also illustrates that even within propagation windows, there are narrow wavelength bands of high absorption. This makes characterizing the effects of absorption and scattering heavily dependent on the wavelength of the light. Furthermore,

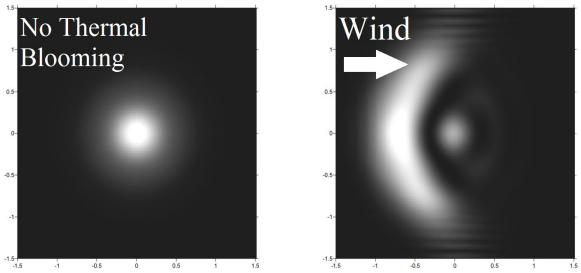

FIGURE 3.3 The Gaussian irradiance pattern on the left is unaltered with beam power shown in white. On the right, an incoming cross wind from the left bends the irradiance pattern into a characteristic crescent shape. Adapted from [14].

the attenuation coefficient ϵ is often a function of position. This dependence on position arises from its dependence on the density of particles present in the beam path, which can change significantly with altitude and other factors. With ϵ as a function of position, Equation 3.1 is re-written

$$P(z) = P(0) \exp\left(-\int \epsilon(z) dz\right)$$

where z is the position along the beam path.

3.2 Thermal Blooming

The effects considered thus far have been linear, meaning the beam power at the target scales proportionally with the initial power of that beam at the source. In contrast, thermal blooming is a nonlinear phenomenon since its effect is dramatically pronounced as beam power increases.

Thermal blooming is a result of the changing physical characteristics of the air as light propagates through it. As a light beam's energy is absorbed by air, the temperature of the air increases. This increase in temperature causes the air to expand as hot air is less dense than cold air. The air in the beam's path therefore becomes less dense where the beam power is greater. This density differential causes a variation of the index of refraction within the beam cross section, with a lower index where the air is warmer, producing a diverging lens effect that widens the beam. Cross winds replace heated air along the beam path with cooler air. These cross winds cause the beam to bend upwind where the index of refraction of the cooler, incoming air is greater. The effect of cross winds on beam irradiance is shown in Figure 3.3.

To investigate the magnitude of the effect of thermal blooming, consider a beam propagating through a uniform atmosphere. The amount of blooming is approximately characterized by the dimensionless *thermal distortion factor*, N_D. Assuming equal weighting along the path, N_D is given by

$$N_D \approx -\frac{4\sqrt{2}kPn_T\alpha \mathrm{T}}{\rho_0 C_p D V_{\text{wind}}} R. \tag{3.2}$$

where $k = 2\pi/\lambda$ is the wave number, P is the laser power, $n_T = dn/dT$ is the rate at which index of refraction changes as a function of temperature, α is the absorption coefficient, T is the transmittance, ρ_0 is the density of air, C_p is the heat capacity of air, D is the beam diameter, V_{wind} is the effective wind speed perpendicular to the beam, and R is the total slant path length of the beam. The effect of thermal blooming becomes significant when $N_D > 25$ [15].

The higher the thermal distortion factor, the more distorted the beam becomes. Note the direct proportionality of N_D with P. This characteristic means that the naive action of increasing power to compensate for the effects of thermal blooming may actually exacerbate the problem. At high N_D, increasing P will more rapidly decrease the irradiance on target. The power that produces maximum irradiance on target is known as the critical power, P_{crit}, and is estimated by the equation

$$P_{\text{crit}} = \left(\frac{P}{N_D}\right)\left(\frac{-1}{a(1-m)}\right)^{1/m} \tag{3.3}$$

where a and m are parameters that describe the intensity profile of the beam. For a Gaussian beam, $a = 0.0625$ and $m = 2$ [15]. For a typical laser beam and atmospheric conditions, P_{crit} is on the order of hundreds of kilowatts. Figure 3.4 shows how increasing the output power of a laser will increase the irradiance on target until $P = P_{\text{crit}}$; beyond that level, increasing output power will begin to reduce irradiance on target. Note that while the calculation for P_{crit} in Equation 3.3 appears to be proportional to the laser power itself, the thermal distortion factor is also directly proportional to laser power P, so the laser power factor in P_{crit} cancels.

3.3 Turbulence

Atmospheric turbulence begins with random temperature fluctuations that originate from convection and wind shear and cause air density inhomogenieties. These inhomogeneities cause index of refraction variations that bend and distort light. The air pockets of varying

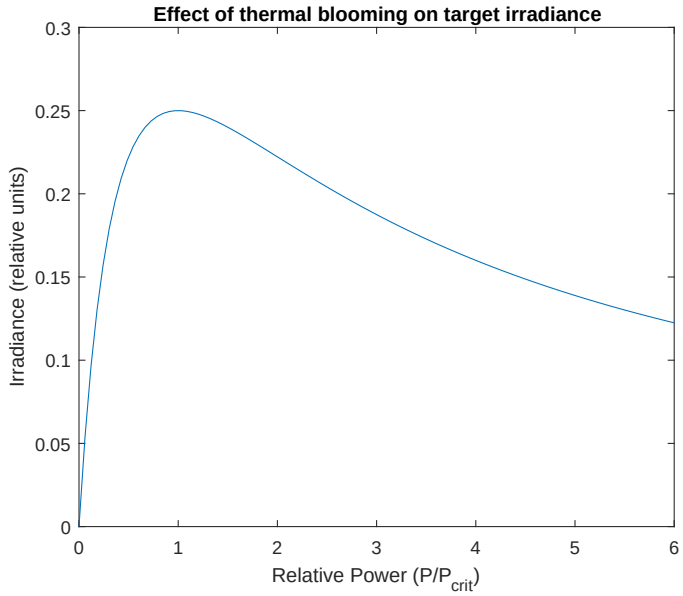

FIGURE 3.4 Plot of irradiance on target as a function of laser power. Continuing to increase laser power will decrease irradiance on target beyond the value of P_{crit}. The value of P_{crit} is specific to the atmospheric conditions in which the laser is operating. Adapted from [16].

density, called turbulence cells, affect laser propagation by effects known as beam wander and scintillation.

3.3.1 Characterization of Turbulence

Characterization of turbulence is complicated by nonuniform weather conditions in the atmosphere that results in inhomogeneous and anisotropic turbulence cells [17]. Despite this, statistical models can approximate small-scale turbulence to be homogenous, isotropic, and ergodic, meaning that turbulence on that scale is independent of local position, direction, and time, respectively [15]. The upper size-limit to this homogeneous approximation is the outer scale of turbulence, L_0. The magnitude of L_0 can be about 20% of the height above the ground, but is generally not larger than 100 m [17]. These larger wind eddies transfer energy to smaller eddies, creating turbulence cells of various size. This cascading effect ends in viscous dissipation at the smallest size-scale, whereby kinetic energy transfers into thermal energy. The size of the eddies at which viscous dissipation occurs, characterized by the variable l_0, changes with temperature, pressure, humidity, and wind speed, but the eddies are generally on the order of 1 mm near the surface of the Earth to 1 cm in the tropopause [17]. Figure 3.5 illustrates this effect.

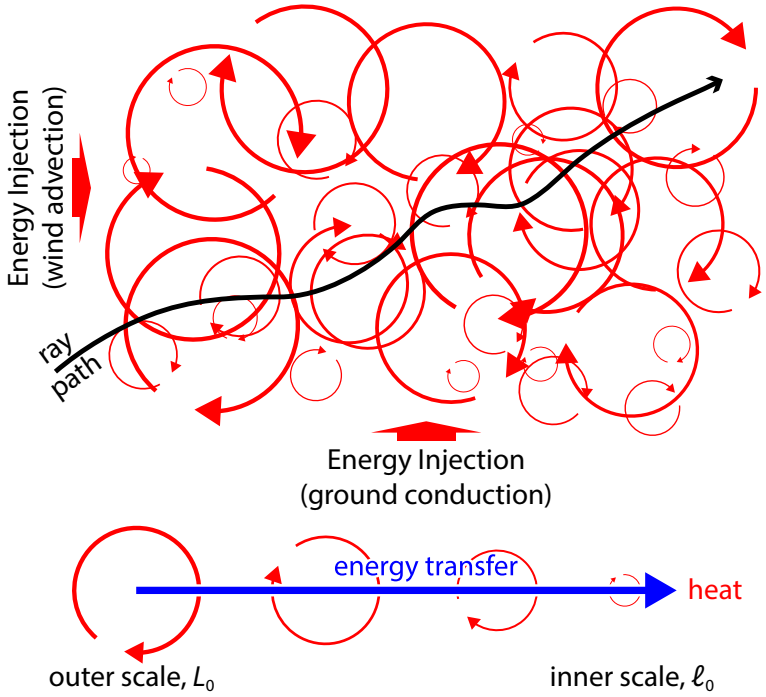

FIGURE 3.5 The cascading effect of energy as it transfers from kinetic energy in large wind eddies of size L_0 into thermal energy through viscous dissipation of smaller eddies with size l_0.

The most ubiquitous parameter describing turbulence is C_n^2, the refractive index structure coefficient, and is governed by pressure and temperature differences that create index of refraction differences between two points. An intuitive understanding of C_n^2 comes from its relation to the structure function, $D_n(r)$, which characterizes how much index of refraction changes over a displacement of length r. The structure function is defined as

$$D_n(r) = \left\langle |n(r_1) - n(r_1 + r)|^2 \right\rangle \tag{3.4}$$

where r_1 is the starting position, r is the distance from r_1 over which the structure function is being measured, n is the index of refraction, and $<| \ldots |^2>$ denotes the averaging over r. A statistical model developed by Kolmogorov defines D_n as a function of C_n^2 [18]:

$$D_n(r) = \begin{cases} C_n^2 l_0^{-4/3} r^2 & 0 \le r \ll l_0 \\ C_n^2 r^{2/3} & l_0 \ll r \ll L_0 \end{cases}. \tag{3.5}$$

A C_n^2 value on the order of $10^{-17}\ \mathrm{m}^{-2/3}$ corresponds to weak turbulence, while a C_n^2 value on the order of $10^{-13}\ \mathrm{m}^{-2/3}$ corresponds to strong turbulence [17].

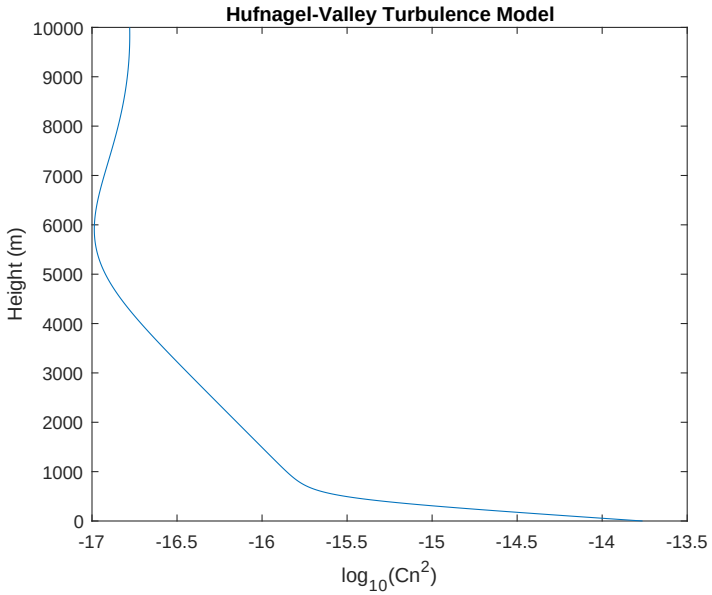

FIGURE 3.6 The Hufnagel-Valley model roughly characterizes values of the refractive index structure coefficient as a function of altitude. Near the surface of the Earth, C_n^2 is larger because the influence of convection from the ground on turbulence is more significant than it is at higher altitudes. Adapted from [19].

One of the standard models that characterizes C_n^2 with respect to height is the Hufnagel-Valley Turbulence Model [19], shown in Figure 3.6. This model follows the typical trend of larger C_n^2 values near the surface of the Earth where the effects of convection from the ground heavily influence atmospheric conditions.

Another common parameter used to describe turbulence over a path is the Fried coherence length, r_0. The Fried coherence length is the transverse distance over which a beam of light will remain coherent and is a function of a specific path through the atmosphere. Coherent light here is generally considered to be light that is in phase within a root-mean-square difference of 1 radian [15]. The Fried parameter is given by [20]

$$r_0 = \left[\frac{2.905}{6.88} \left(\frac{2\pi}{\lambda} \right)^2 \int_0^R C_n^2(z) dz \right]^{-3/5} \qquad \text{[plane wave]}$$

and

$$r_0 = \left[\frac{2.905}{6.88} \left(\frac{2\pi}{\lambda} \right)^2 \int_0^R C_n^2(z) \left(\frac{R-z}{R} \right) dz \right]^{-3/5} \qquad \text{[spherical wave]}$$

where z is the position along the path, R is the total path length, and the additional term in the integral for a spherical wave accounts for the reduced beam area affected by the turbulence [15]. If a constant C_n^2 is assumed along the beam path for each of these waves, the Fried parameters become

$$r_0 = 0.185\frac{\lambda^{6/5}}{R^{3/5}(C_n^2)^{3/5}} \quad \text{[plane wave]} \tag{3.6}$$

and

$$r_0 = 0.33\frac{\lambda^{6/5}}{R^{3/5}(C_n^2)^{3/5}} \quad \text{[spherical wave]}. \tag{3.7}$$

Small Fried parameters indicate strong turbulence. Conversely, larger Fried parameters indicate weak turbulence. A laser with a wavelength $\lambda \approx 1\,\mu$m represented by a spherical wave and fired across a range of R = 5 km would experience $r_0 \approx 1$ cm for strong turbulence ($C_n^2 = 10^{-13}\,\mathrm{m}^{-2/3}$) and $r_0 \approx 2$ m for weak turbulence ($C_n^2 = 10^{-17}\,\mathrm{m}^{-2/3}$). In the limit of weak turbulence where the diameter of the beam director D is less than the Fried parameter, the angular divergence of an ideal beam is approximately diffraction-limited at

$$\theta \backsim \frac{\lambda}{D}.$$

In the limit of strong turbulence where $D > r_0$, the angular resolution becomes atmospherically-limited:

$$\theta \backsim \frac{\lambda}{r_0}. \tag{3.8}$$

Therefore, a laser beam coming from an aperture larger than r_0 will suffer a significant reduction in irradiance due to turbulence.

An additional parameter closely related to r_0 is the isoplanatic angle, θ_0, which is the angle subtended by r_0 over the path of interest. The isoplanatic angle is given by [21]

$$\theta_0 = \left[2.905k^2 \int_0^R C_n^2(z) z^{5/3} dz\right]^{-3/5}, \tag{3.9}$$

which for a constant value of C_n^2 becomes

$$\theta_0 = 0.314\frac{r_0}{R}.$$

The isoplanatic angle is a useful parameter because it defines a region within which

turbulence leads to negligible phase differences. In order to correct for the effects of atmospheric turbulence on a laser with adaptive optics, the path of the laser beam must fall within the isoplanatic angle of the corrected path [21].

Finally, the Greenwood frequency is a measure of how quickly a control system must correct for turbulence in the atmosphere. Calculating the Greenwood frequency relies on Taylor's frozen cell hypothesis [22], which assumes that turbulence cells are carried unchanged by the wind. The Greenwood frequency is calculated by the expression

$$f_G = \left[0.102k^2 \int_0^R C_n^2(z) V_{\text{wind}}^{5/3}(z) dz \right]^{3/5} \tag{3.10}$$

where $k = 2\pi/\lambda$ is the wave number, V_{wind} is the wind speed, and z is the position of the beam along the path. Equation 3.10 becomes

$$f_G = 0.421 \frac{V_{\text{wind}}}{r_0}$$

for constant V_{wind} and C_n^2 along the path. It is important to note that V_{wind} is the speed of the air in the plane perpendicular to the axis of laser transmission. In the application of laser weapons, the relative motion between a laser and a target will manifest in this term. For example, a laser propagating along a path of constant C_n^2, an r_0 of 1 m, and through a V_{wind} of 20 m/s will encounter a Greenwood frequency of $f_G \approx 10$ Hz.

3.3.2 Effects of Turbulence on Propagation

The effect that turbulence has on the laser beam depends on the size of the turbulence cells. At the upper limit of cell size where the cells are larger than the width of the propagating beam, a phenomenon known as "beam wander" occurs that randomly causes the entire beam to move about the aim point. At the lower limit of smaller turbulent cells, "scintillation" becomes significant, which describes the laser beam breaking up into beamlets by the time is reaches the target. In weak turbulence ($C_n^2 \sim 10^{-17}\,\text{m}^{-2/3}$), beam wander is the prominent effect, whereas both effects are present in strong turbulence.

Temperature gradients in the atmosphere result in refractive index inhomogeneities that cause a single beam to break up into multiple smaller beamlets through a time-dependent effect known as scintillation. Figure 3.7 is a comparison of two irradiance patterns that shows this effect. Diffraction plays a significant role in scintillation. A small turbulence

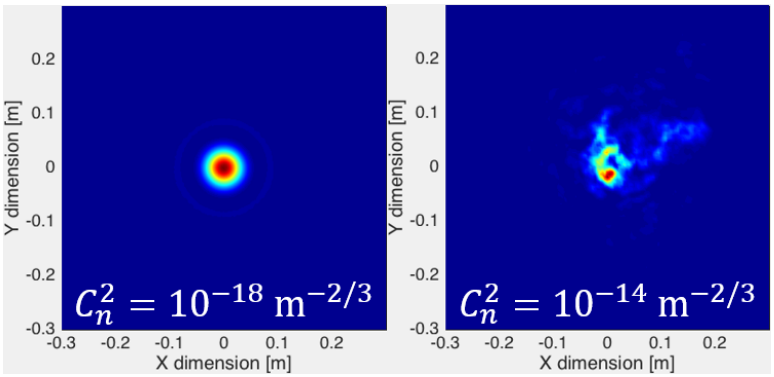

FIGURE 3.7 On the left is the simulated irradiance pattern on target of a laser affected by an atmosphere with weak turbulence. Conversely, the pattern on the right is greatly distorted by a turbulent atmosphere represented by a C_n^2 value that is four orders of magnitude larger. Source: [23].

cell in the atmosphere will cause beam spreading according to $\theta \simeq \lambda/l$ where l is the size of the turbulence cell and θ is the diffraction angle. As the turbulence cells become smaller, the angle at which light is diffracted from its intended path becomes larger and the final irradiance on target becomes more distorted. The maximum diffraction angle occurs for the smallest turbulence cells of size l_0, where $\theta_{max} \approx \lambda/l_0$.

Turbulence can be described by its contribution to the resulting time-averaged spot size of a laser on target. This concept will be discussed in further detail in Section 5.1, but suffice it to say that smaller spot size contribution terms are better than larger terms for directed energy applications. The target spot size in a vacuum is adapted from Breaux's formulation and described by [24]

$$a_d^2 = 0.5\left(\frac{m' M^2 \lambda z}{D}\right)^2 \tag{3.11}$$

where m' is characteristic of the beam shape as listed in Table 3.1, M^2 is a measure of beam quality ($M^2 = 1$ represents an ideal beam), λ is the wavelength of the laser beam, z is the propagation distance, and D is the laser beam director diameter. The spot size contribution of turbulence is a function of a_d^2 and is approximated

$$a_{tt}^2 = \left(\frac{a_d}{M^2}\right)^2 \left(\frac{D_e}{r_0}\right)^2$$

where D_e is the effective aperture size appropriate to the beam shape as listed in Table 3.1. The total turbulence spot size contribution incorporates the effects of both scintillation

TABLE 3.1 Values for m' and D_e^2 as they relate to various beam shapes. Adapted from [24].

	m'	D_e^2
infinite Gaussian beam	$2/\pi$	$2D^2$
truncated Gaussian beam	0.9166	$0.925D^2$
uniform beam	0.9202	D^2

and beam wander. Scintillation occurs over scale sizes that are small relative to the cross section of a laser. Conversely, beam wander occurs over scale sizes that are large relative to the cross section of a laser. When considering large-scale effects to be mitigated by a fast steering mirror, a_{tt}^2 reduces to the short-term turbulence contribution term a_t^2, which is also a function of a_d^2 and is estimated by

$$a_t^2 = \begin{cases} 0.182(a_d/M^2)^2(D_e/r_0)^2 & \text{for } (D_e/r_0) < 3 \\ (a_d/M^2)^2[(D_e/r_0)^2 - 1.18(D_e/r_0)^{5/3}] & \text{for } (D_e/r_0) > 3 \end{cases} \tag{3.12}$$

Table 3.1 contains values for m' and D_e^2 as they relate to various beam shapes. The goal of adaptive optics is to compensate for the small-scale effect of scintillation in order to reduce a_t^2.

CHAPTER FOUR

Adaptive Optics

Adaptive optics (AO) systems were developed to mitigate the detrimental effects of atmospheric turbulence on light beam propagation. AO systems have a variety of different designs, but they all address the issue of turbulence and apply similar logic in correcting for its effect. We will explore the conditions under which AO systems are useful and provide the details of the system components.

4.1 The Need for Adaptive Optics

In the previous chapter, we concluded by quantifying the effects of turbulence in terms of spot size contribution. The target spot size in a vacuum, a_d^2, is imposed by diffraction and is the lower physical limit of total target spot size. The spot size contribution resulting from atmospheric turbulence, a_t^2, is in addition to the diffraction variance. If the condition $a_t^2 \gg a_d^2$ is met, the total spot size is dominated by turbulence and AO can be useful in improving beam quality. When $a_d^2 \gg a_t^2$, the total spot size is diffraction-dominated, so AO would not be as helpful a component of the overall HEL system. Consider typical values for an ideal HEL modeled as a truncated Gaussian ($m' = 0.9166$ and $D_e^2 = 0.925D^2$ from Table 3.1, $M^2 = 1$) with a beam director diameter $D = 50\,\text{cm}$ and wavelength $\lambda = 1\,\mu\text{m}$ propagating $R = 5\,\text{km}$ through an atmosphere of constant intermediate turbulence, $C_n^2 = 5 \times 10^{-15}\,\text{m}^{-2/3}$. Using Equation 3.7 with these parameters yields $r_0 \approx 5\,\text{cm}$. Going on to calculate each component of the spot size terms with Equations 3.11 and 3.12 yields approximate values of $a_d^2 \approx 4.2 \times 10^{-5}\,\text{m}^2$ and $a_t^2 \approx 1.9 \times 10^{-3}\,\text{m}^2$. These values indicate that turbulence is significant for this reasonable case.

A similar condition used to determine when AO would be useful is the relation between the Fried parameter, r_0, and the beam director diameter, D. When $r_0 \lesssim D$, turbulence is significant. This condition is also met with the given parameters, so we can see that this HEL operating in this plausible environment experiences significant turbulence that can potentially see improvement with the use of adaptive optics.

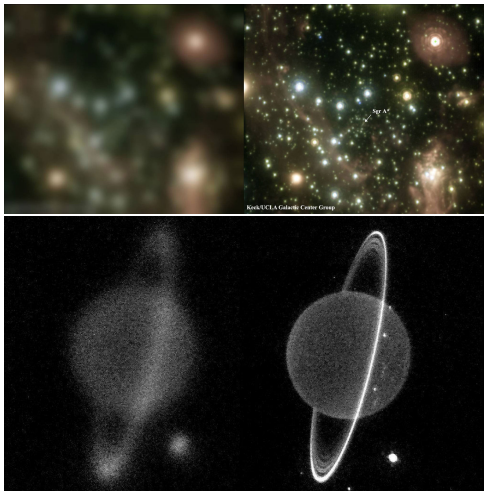

FIGURE 4.1 Two sets of images showing the effect of AO taken at the Keck Observatory. For each set, the left image is taken without AO and the right image is taken after the AO corrections are applied. Top: The center of the Milky Way galaxy. Bottom: An image of Uranus. Source: [1].

4.2 Adaptive Optics Overview

Before describing particular AO system components and setups, it is useful to outline the logic used in developing these systems. We have established how turbulence perturbs a wavefront, which disrupts the focus of the beam on target. In astronomy, the target is an imaging sensor and the source is an astronomical object, while in the application of laser weapons, the target is an enemy asset and the source is the laser. In both applications, it is highly desirable to reconstruct the beam quality of the original source before turbulence perturbed the wavefront. If we use a deformable mirror in the optics chain to impose the opposite of the phase disturbance induced by turbulence, then we can reverse the effects of turbulence. This process requires a means of measuring and characterizing the phase of the wavefront perturbed by turbulence. Assuming turbulence-induced wavefront perturbations can be measured, an AO system also would require a feedback loop to reshape the deformable mirror to cancel as much of these perturbations as possible. Adaptive optics systems are often closed loop, meaning the effect of the correction applied by the deformable mirror is detected by the wavefront sensor and read into future commands to the deformable mirror [21].

While AO in laser weapons is still a developing field, the technology has been used for several decades on telescopes in astronomy to increase image resolution. Two sets of images that show the improvement of AO on beam quality are given in Figure 4.1.

4.3 Characterizing Wavefront Error

Opticians classify several types of monochromatic optical aberrations, including spherical aberration, astigmatism, coma, field curvature, and distortion [25]. In the application of AO, it is necessary to understand these aberrations mathematically. Zernike polynomials form a convenient orthonormal basis set defined on a unit circle, making them useful in describing an aberrated wavefront.

The Zernike polynomials, pictured in Figure 4.2, are grouped into even and odd polynomials that are defined as

$$Z_n^m(\rho, \theta) = R_n^m(\rho)\cos(m\theta) \tag{4.1}$$

for even polynomials and

$$Z_n^{-m}(\rho, \theta) = R_n^m(\rho)\sin(m\theta) \tag{4.2}$$

for odd polynomials where n and m are the radial and azimuthal mode orders respectively, ρ and θ are polar coordinates on the unit circle, and R_n^m is the radial Zernike polynomial defined in Equation 4.3 [26]. For these definitions of Zernike polynomials, positive superscripts correspond to even Zernike polynomials and negative superscripts correspond to odd Zernike polynomials. It is important to note that even when the superscript for odd Zernike polynomials is negative, the m value used to calculate the polynomial is positive. The mode orders n and m are non-negative integers constrained by the conditions $m \leq n$ and $n - m =$ even. With these constraints, a sequence of ordered index pairs can be listed by increasing the value of n and then stepping through each possible value of m. Often, the ordered pairs are sequentially assigned the mode order j. A list of the first 10 Zernike polynomials is shown in Table 4.1.

The index, j, is useful for applying Zernike polynomials to characterize atmospheric turbulence. Additionally, modified normalization constants are introduced for reasons of simplicity in statistical analysis that redefine Zernike polynomials as [27]

$$Z_j(r, \theta) = \begin{cases} \sqrt{n+1}R_n^m(r)\sqrt{2}\cos(m\theta) & j \text{ even, m} \neq 0 \\ \sqrt{n+1}R_n^m(r)\sqrt{2}\sin(m\theta) & j \text{ odd, m} \neq 0 \\ \sqrt{n+1}R_n^0(r) & m = 0 \end{cases}.$$

The radial Zernike polynomials are defined as [27]

$$R_n^m(r) = \sum_{s=0}^{(n-m)/2} \frac{(-1)^s(n-s)!}{s![(n+m)/2-s]![(n-m)/2-s]!} r^{n-2s}. \tag{4.3}$$

The mode orthogonality can be succinctly written

$$\int d^2r\, W(r) Z_j Z_{j'} = \delta_{jj'}$$

where

$$W(r) = \begin{cases} 1/\pi & \text{for } r \leq 1 \\ 0 & \text{for } r > 1 \end{cases}.$$

If the phase of an electric field is represented as a three-dimensional surface where peaks and troughs represent phase advance and retardation, respectively, the Zernike series used to describe that surface can be written as

$$\phi(\rho, \theta) = \sum_j a_j Z_j(\rho, \theta) \tag{4.4}$$

where $\rho = r/R$ is the normalized radial coordinate, R is the radius of the circle over which the series is defined, and a_j are coefficients defined as

$$a_j = \left(1/R^2\right) \int_0^R d^2r\, W(\rho) \phi(\rho, \theta) Z_j(\rho, \theta).$$

Tying the mathematical descriptions to a more qualitative understanding of optical aberrations, piston is represented by the first Zernike polynomial ($j = 1$) and the x and y coordinates of tilt are represented by the second ($j = 2$) and third ($j = 3$) Zernike polynomials, respectively. Defocus is represented by the radially symmetric fourth ($j = 4$) Zernike polynomial. The higher order effect of astigmatism is represented by the ($j = 5$) and ($j = 6$) Zernike polynomials while coma is shown by the ($j = 7$) and ($j = 8$) polynomials [28].

While AO can presumably correct for some number of Zernike polynomials, the remaining wavefront is still represented by the residual error, which is conveniently represented with Zernike polynomials by

$$\Delta_j = \left\langle \phi^2 \right\rangle - \sum_{j=1}^{J} \left\langle |a_j|^2 \right\rangle \tag{4.5}$$

where $\left\langle \phi^2 \right\rangle$ is the phase variance and J is the number of corrected Zernike polynomials. Noll provides the values of residual error up to Δ_{21}. For a wavefront aberrated by turbulence, the residual variance is

$$\Delta_j \approx 0.2944 J^{-\sqrt{3}/2} (D/r_0)^{5/3}$$

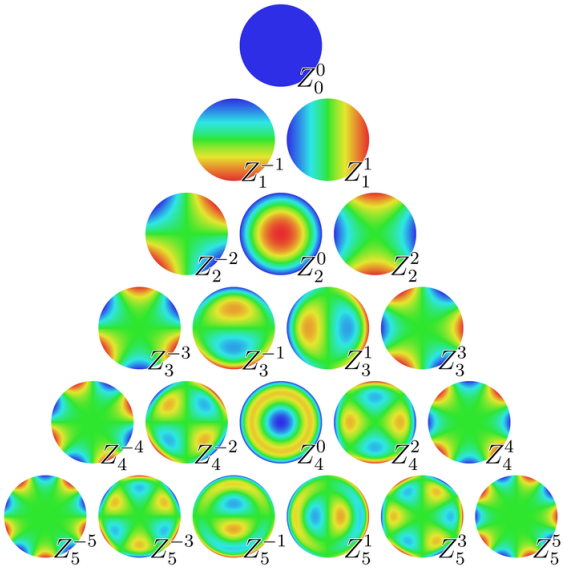

FIGURE 4.2 Graphical representations of 21 Zernike polynomials listed with the modal numbers n and m used to generate them. Source: [29].

TABLE 4.1 The radial, n, and azimuthal, m, mode order combinations used to produce the first 10 Zernike mode orders, j. Adapted from [27].

Z_n^m	Z_0^0	Z_1^1	Z_1^{-1}	Z_2^0	Z_2^{-2}	Z_2^2	Z_3^{-1}	Z_3^1	Z_3^{-3}	Z_3^3
j	1	2	3	4	5	6	7	8	9	10

when $J > 10$ [27].

4.4 System Components

Conventional AO systems consist of three basic components: a wavefront sensor, a control computer, and a deformable mirror. The basic steps in the corrective process are to measure the phase of the beam with the wavefront sensor, compute the necessary deformable mirror compensation, and then apply the compensation.

While the logic underpinning various AO systems is the same, different applications require different configurations of the system components. The diagram on the left of Figure 4.3 shows the most common type of AO in use today, which is the configuration used for astronomical imaging [21]. A guide star of some sort emits coherent light from outside of the turbulent atmosphere and along a propagation path within the isoplanatic angle of the object. The perturbed light is measured by the wavefront sensor and the conjugate of

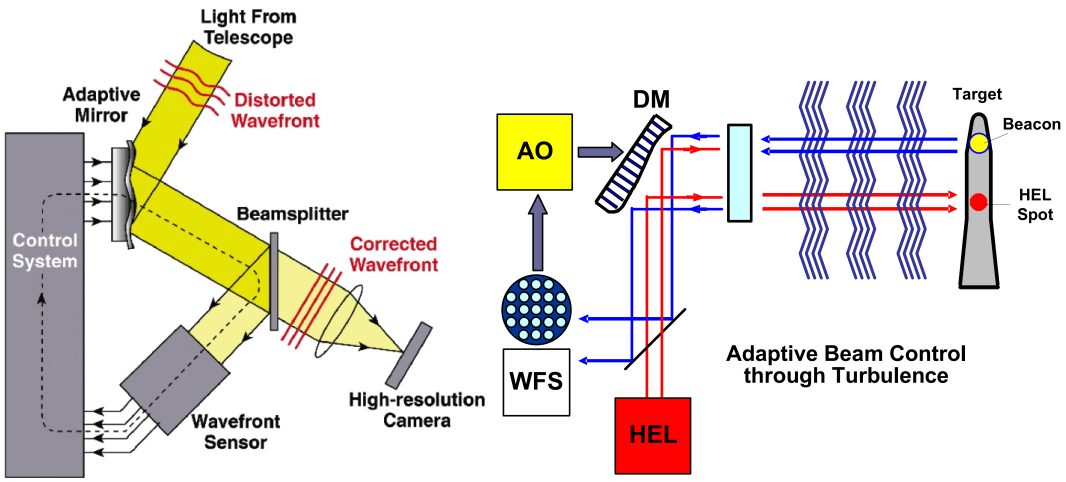

FIGURE 4.3 Left: The most common AO configuration, used for astronomical imaging, in use today. Right: The configuration of AO in laser weapon systems requires light returned from the target to characterize atmospheric turbulence. Sources: [23], [30].

the wavefront error is applied by actuators in the deformable mirror. The correction to the guide star light beam is then applied to later wavefronts from both the guide star and imaging object entering the optics chain. If this loop occurs faster than the characteristic turbulence changes ($f_{BW} > f_G$ where f_{BW} is the frequency bandwidth of the AO system and f_G is the Greenwood frequency), image resolution will improve.

The configuration used in the application of laser weapons has slight variations from that shown on the left of Figure 4.3. Laser weapon AO systems differ primarily in their source of reference light and the location of the applied correction in the optics chain. While imaging systems use a guide star or other source as a reference to measure turbulence, laser weapons measure the wavefront of light returning from a target object. It is not necessary to use the return from the high average power laser light itself in the wavefront compensation measurements. Instead, a collinear pulsed laser with a different wavelength and lower average power but higher peak power can be used. The wavefront of the reference pulsed laser will be distorted differently than the wavefront of the HEL, but the difference can be compensated for by a gain factor in the correction algorithm [21]. Moreover, the deformable mirror in an imaging system applies a correction to incoming light shortly before it is imaged. Conversely, the deformable mirror in the AO system of a laser weapon preforms the phase front of the outgoing laser beam, effectively using the turbulent atmosphere to apply a correcting effect to the beam as it reaches its target. The AO configuration generally used in laser weapons systems is shown on the right of Figure 4.3. In addition to partially correcting the abberation induced by atmospheric turbulence,

AO systems can passively mitigate static abberation caused by misalignment, imperfection, or damaged surfaces in the optical system.

4.4.1 Wavefront Sensor

The phase of a light beam is not directly measurable because photo sensors respond to irradiance, which is proportional to the square of the complex field. Several methods have been developed to measure the phase of a light beam indirectly by measuring tilt and curvature [31], [32].

The propagation direction of a light beam can be described by a vector normal to the surface of its wavefront. Take, for simplicity, an unaberrated wavefront. If this light beam were to pass straight through a lens, it would focus to a spot on the optical axis of that lens. If, however, this light beam were to pass through the lens at some small angle from the optical axis, the spot on the focal plane would move a distance away from the optical axis proportional to the light beam's tilt. The geometry of light beam tilt is shown in Figure 4.4.

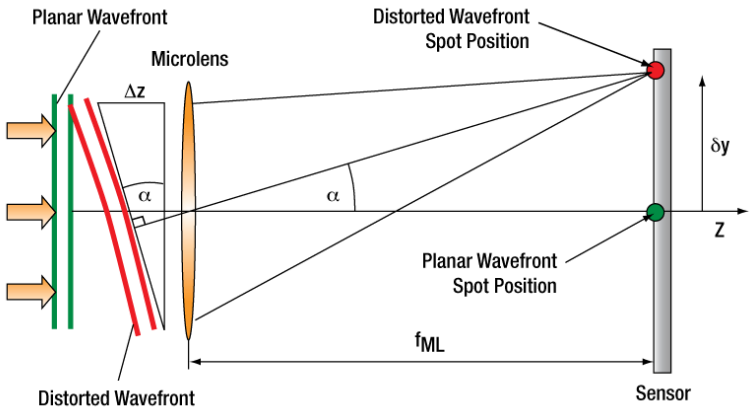

FIGURE 4.4 A tilted wavefront will focus to a spot on the focal plane that is a distance δy away from the optical axis, z. This shift is proportional to the tilt, α. Source: [33].

By placing a sensor along the focal plane to detect the position of the spot, the tilt of the unaberrated wavefront, or average tilt of an aberrated wavefront, can be directly measured. One sensor used to measure the spot position is the quadcell, which consists of four detectors arranged like quadrants on two-dimensional axes. The difference between the average signal in the two left detectors and the average signal in the two right detector gives the horizontal position of the spot. Similarly, the difference between the average signal in the two upper detectors and the average signal in the two lower detectors gives the

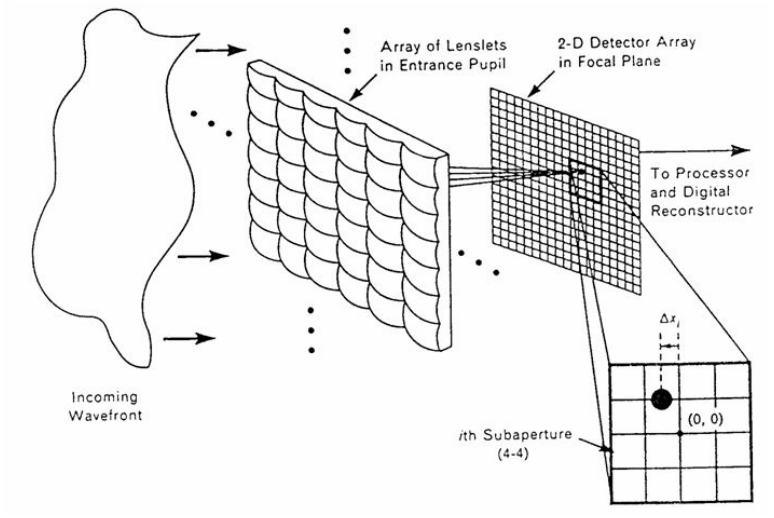

FIGURE 4.5 The Hartmann sensor, sometimes called the Hartmann-Shack sensor, breaks a beam into constituent beamlets with an array of lenses and measures the tilt of each beamlet with a CCD or similar sensor. Source: [34].

vertical position of the spot . The Hartmann wavefront sensor, shown in Figure 4.5, extends this technique of measuring wavefront tilt by breaking a light beam into constituent beamlets with an array of lenses. The focused spots are detected by a CCD or an array of quadcells and the wavefront tilts of each beamlet collectively form an approximation for the wavefront of the overall beam [31].

Another method of measuring tilt (or first derivatives of the wavefront) uses shearing interferometry. Interferometry makes use of the relation between interference pattern intensity and phase. The first experiment characterizing this wave property of light was conducted by Young in his famous double-slit experiment [35]. Through the interference of light beams, phase information is translated into intensity variations. A common type of interferometer used in adaptive optics is a shearing interferometer, which interferes a light beam with a displaced replica [36]. The intensity pattern that results from this interference is proportional to the displacement, or shearing distance, multiplied by the cosine of the slope, or the tilt [21]. Characterizing the full wavefront requires two measurements from shearing in two orthogonal directions to measure the slopes in each direction. By measuring the interference pattern and shearing distance, the shearing interferometer delivers the wavefront tilt. A general setup and the extracted phase information are shown in Figure 4.6.

While Hartmann-Shack sensors and shearing interferometers measure first derivatives, a

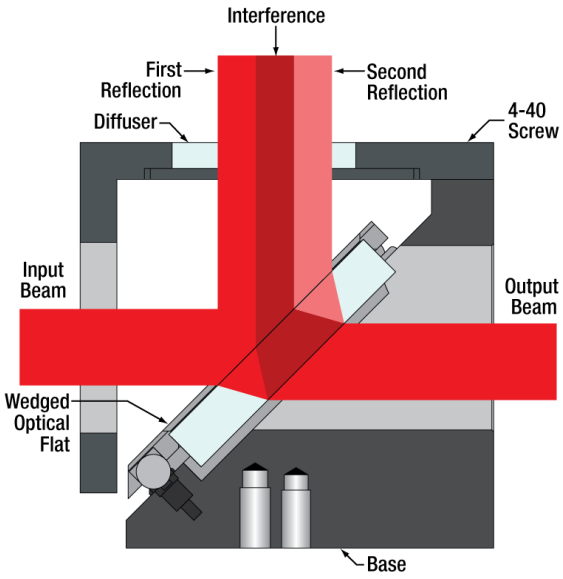

FIGURE 4.6 The shearing interferometer measures the phase difference between a light beam and a displaced replica of that beam. Source: [37].

wavefront can also be characterized by its curvature. One approach to measuring wavefront curvature directly uses an array of lenses, similar to that of a Hartmann-Shack sensor, to break a light beam into constituent beamlets. The difference between signals collected from two sensors on either side of the focal plane of the lenses correspond to the local curvature of the beam [32]. Curvature measurements are especially useful in adaptive optics systems that use bimorph deformable mirrors, which produce curvature deformations [21].

4.4.2 Deformable Mirror

In addition to the deformable mirror, most AO systems have a separate tilt mirror in the optics chain to remove the overall light beam tilt, which aside from piston is the lowest mode of optical aberration. Some adaptive optics systems also contain a secondary mirror that can move along the optic axis of the beam to control focus.

There are generally two kinds of deformable mirrors: segmented and continuous faceplate, shown in Figure 4.7. The number of actuators on segmented mirror plates determines the allowed motion of each segment. One actuator per mirror adjusts beam translation in the piston mode. Three or more actuators per mirror can adjust the tilt mode at each segment. Actuators also fall into two categories: displacement actuators and force actuators. Actuators commonly push and pull the mirror surface in a direction transverse to the mirror surface. Perhaps the most commonly used are displacement actuators that make

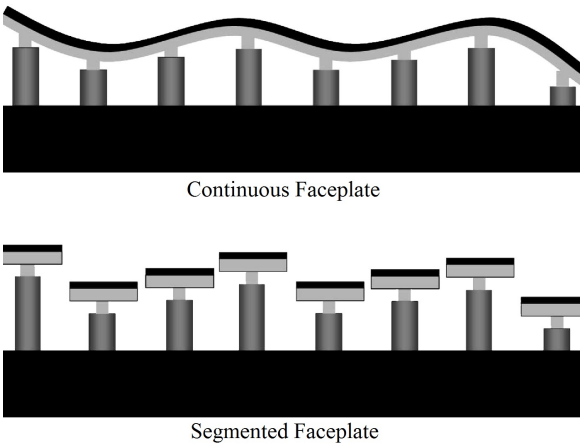

FIGURE 4.7 Schematics of two main kinds of deformable mirrors. Top: Some coupling exists between the actuators of a continuous faceplate mirror, resulting in a more complicated mirror response to the application of one actuator. Bottom: The segmented faceplate mirror pictured has one actuator per segment, which only provides correction of the piston mode. Source: [38].

use of the piezoelectric effect with materials such as lead zirconate titanate (PZT) and lead magnesium niobate (PMN) [39][40]. In the case of a continuous faceplate mirror, each actuator will have some influence on the surrounding surface. The total deformation caused by a single actuator is modeled by "influence functions" [41]. Another closely related concept is coupling, which is the height of the mirror at actuators surrounding the actuator that applied pressure to the mirror, but is often expressed as a percent. Mirror coupling ranges from zero percent for segmented mirrors, a few percent for a thin mirror, to 10-20 percent for commonly used DM [21]. All other things being equal, thicker mirrors will have more coupling. Low coupling permits higher order aberration correction, but requires a larger number of actuators to implement. High coupling results in smoother surfaces transitions that can benefit lower order mode correction. Actuators often respond differently in different directions of motion, an effect called hysteresis. The position-dependence of the mirror on the applied actuator direction is a concern in any AO system with actuator materials that exhibit hysteresis. While it can be reduced by calibration, the effect of hysteresis ultimately lowers the control bandwidth of the AO system.

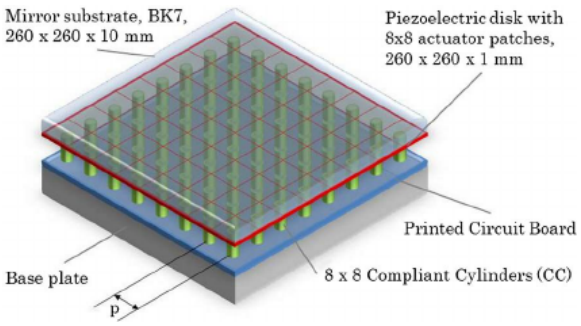

FIGURE 4.8 Deformable mirror schematic with a square grid of 64 piezoelectric actuators. Source: [42].

Other types of deformable mirrors include bimorph and micro-electro-mechanical (MEM) deformable mirrors [43][44]. Bimorph mirrors use two surfaces that expand and contract differently in the presence of an applied electric field and deform the curvature of the mirror surface. Recently developed MEM deformable mirrors contain hundreds of actuators with high control bandwidths and low hysteresis, all of which are ideal parameters for accurate reconstruction of higher mode order aberrations.

4.4.3 Control Computer

Adaptive optics systems can be described by their relative number of wavefront sensor measurements and actuators. A system with fewer wavefront sensor measurements than actuators will experience difficulty in determining appropriate actuator commands and is called “underdetermined”. If the system has an equal number of both, it is “determined” and each wavefront measurement can be directly paired with an actuator. Most systems are “overdetermined”, meaning there are more signals coming from the wavefront sensor than there are actuators to implement the required deformation. In any case, the control computer converts electrical signals from the wavefront sensor into signals to the actuators of the deformable mirror. Another distinguishing factor of actuators is the speed of the response. Faster responses move actuators toward the correct final position more quickly, but too fast a response will cause the actuators to overshoot the final position like an underdamped oscillator. However, if the response is not fast enough, the AO system will perhaps do more harm than good by correcting for the wrong turbulence conditions. Generally, an AO system that does not satisfy the condition $f_{BW} > f_G$ will not be effective. One goal of the control system design is to optimize this AO system response.

In order to quantify the requirements of a control system, we break down a perturbed wavefront into its constituent sine waves using Fourier analysis and analyze the effects

of our control system on each of those waveforms. The AO system will effectively alter the amplitude and shift the phase of many of these constituent sine waves. The ratio of the output amplitude to the input amplitude at each frequency is called the gain. Note that in the control system discussion, frequency (ω) refers to the frequency of a perturbed wavefront component, not the frequency of the light beam. If a single input sine wave is $r(t) = A\sin(\omega t)$, its output is $c(t) = AM(\omega)\sin(\omega t + \phi(t))$ where $M(\omega)$ is the gain and $\phi(t)$ is the frequency-dependent phase shift. Gain is often written in decibels where $M_{\text{dB}} = 20\log M(\omega)$. A plot of these values is called a Bode plot as shown in Figure 4.9 [21].

While the AO system will eliminate some of the unwanted aberration, there will still be some remaining. This remaining aberration is largely a function of the AO system bandwidth, which is the range of frequencies over which the system applies a correction that sufficiently eliminates those frequencies from the perturbed wavefront. For further analysis, it is useful to work in Hz by converting the sinusoidal Fourier components with formula $f = \omega/(2\pi)$. With the equation [35]

$$F(f) = 0.32 f_G^{5/3} f^{-8/3},$$

we can develop a spectrum of turbulence component frequencies that is also a function of the Greenwood frequency, f_G. The portion of the remaining aberration that results from temporal factors is the residual temporal variance, which can now be calculated as [22]

$$\sigma^2_{\text{temp}} = \int_0^\infty [1 - H(f, f_{BW})]^2 F(f) \mathrm{d}f \tag{4.6}$$

where $H(f, f_{BW})$ is a function describing the filter gain with values ranging from 0 to 1. For a perfect step filter, $H(f, f_{BW}) = 1$ when $0 < f < f_{BW}$, indicating that those frequencies are eliminated by the AO system and will make no contribution to the residual temporal variance. Conversely, $H(f, f_{BW}) = 0$ for $f_{BW} < f < \infty$, indicating a full contribution from each of these frequencies to σ^2_{temp}. Solving the integral in Equation 4.6 for this perfect filter yields

$$\sigma^2_{\text{temp}} \approx \left(\frac{f_G}{f_{BW}}\right)^{5/3}. \tag{4.7}$$

for higher-order wavefront variance. While real AO systems will not function as perfect step filters, this approximation will prove to be sufficient.

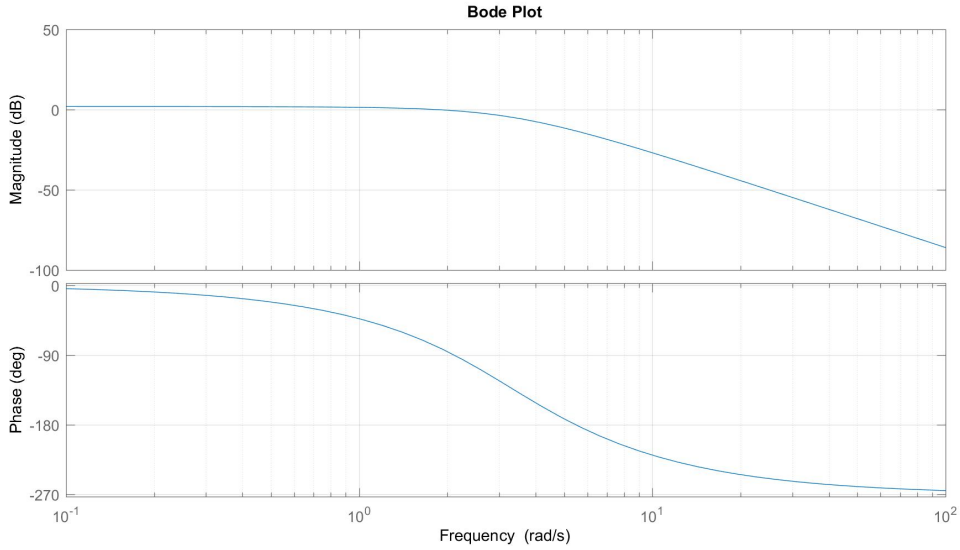

FIGURE 4.9 Bode plot of amplitude and phase responses of the frequencies of the perturbed wavefront components to a deformable mirror correction. Adapted from [45].

THIS PAGE INTENTIONALLY LEFT BLANK

CHAPTER FIVE

HEL Modeling and Simulation

There are two primary types of simulations in use for high energy laser propagation: one using numerical diffraction methods to propagate the the laser beam using the wave equation and the other using scaling laws to find target irradiance. Numerical diffraction codes are higher fidelity than scaling laws, but can take a prohibitively long amount of time for large parameter studies. The quicker, lower fidelity, simulations using scaling laws are accomplished by codes such as ANCHOR, which was developed within the NPS Direct Energy research group. The faster speed of these scaling codes facilitates exploring large, multidimensional design spaces. To study the efficacy of adaptive optics, scaling laws accounting for their benefits will be incorporated into ANCHOR, which will then be used to estimate improvements using adaptive optics for HEL engagements..

5.1 ANCHOR

The ANCHOR code models the effects of diffraction, turbulence, and jitter on laser beam propagation by approximating their effects on target spot size a^2, which is then used to estimate target irradiance. Each effect contributes a term to the total spot size such that [16]

$$a^2 = a_d^2 + a_j^2 + a_t^2 \tag{5.1}$$

where a_d^2, a_j^2, and a_t^2 are the spot size contributions by diffraction, jitter, and turbulence, respectively. The diffraction contribution, following the previous adaptation of Breaux's [24] treatment in Chapter 3, is given in Equation 3.11. This formulation agrees with Gebhardt's [16] work for an infinite Gaussian beam. For simplicity, we look at the case of a uniform beam such that

$$a_d^2 \approx \left(\frac{M^2 z}{kD}\right)^2 \tag{5.2}$$

where M^2 characterizes the beam quality of the source, z is the target range, $k = 2\pi/\lambda$ is the wavenumber, and D is the beam director diameter. The jitter contribution is given

by [16]:

$$a_j^2 = 2\left\langle \theta_x^2 \right\rangle z^2$$

where $\left\langle \theta_x^2 \right\rangle$ is the variance of the single-axis jitter angle and assumed to be isotropic such that $\left\langle \theta_x^2 \right\rangle = \left\langle \theta_y^2 \right\rangle$. The turbulence contribution, a_t^2, is modeled two different ways depending on how much the laser system is designed to mitigate the effect of turbulence. The general expression for the short term turbulence contribution is previously given in Equation 3.12 and restated below for the case of a uniform beam ($D = D_e$):

$$a_t^2 = \begin{cases} 0.182\left(\frac{a_d}{M^2}\right)^2\left(\frac{D}{r_0}\right)^2 & \text{for } \frac{D}{r_0} < 3 \\ \left(\frac{a_d}{M^2}\right)^2\left(\frac{D}{r_0}\right)^2 - 1.18\left(\frac{D}{r_0}\right)^{5/3} & \text{for } \frac{D}{r_0} > 3 \end{cases}, \tag{5.3}$$

where a_d^2 is the diffraction contribution to the spot size, M^2 is the beam quality, D is the beam director diameter, and r_0 is the Fried parameter. This turbulence spot size contribution models the effect of turbulence without adaptive optics partial correction. The expression accounting for partial correction by adaptive optics will be defined as a function of the adaptive optics-corrected Strehl ratio in a later section.

5.2 Modeling Adaptive Optics

As previously discussed, the atmospheric turbulence perturbs the wavefront of the laser beam along the path of propagation. We define a term for the dimensionless phase variance, σ^2, which is zero for an unabberated wave. While adaptive optics can greatly reduce this term on target, physical limitations in each component will apply an imperfect correction, leaving a residual phase variance. Specifically, the wavefront sensor will be limited by its signal-to-noise ratio. The remaining phase variance from this component is approximated by the expression [46][35]

$$\sigma_{\text{WFS}}^2 \approx \frac{4}{\text{SNR}^2}$$

where SNR is the signal-to-noise ratio of the detector. This approximation holds for sensors that measure tilt from light rays coming from a target at infinity.

The deformable mirror will be unable to perfectly match the detected abberation due to having a finite number of actuators, which is captured in the residual wavefront variance term [46][35][47]

$$\sigma_{\text{fit}}^2 \approx \kappa\left(\frac{r_s}{r_0}\right)^{5/3}$$

where κ is a constant that characterizes the response of the turbulence spectrum to the spectrum of the deformable mirror influence functions, r_s is the actuator spacing, and r_0 is the Fried parameter. This approximation is valid for a square arrangement of actuators. Previous research has shown that $\kappa = 0.34$ is applicable to many systems with Gaussian influence.

Finally, the system response will introduce some delay between when an aberration is detected and when the appropriate correction is applied. During this time delay, the turbulence condition that the laser beam will actually experience will have changed by some amount characterized by the Greenwood frequency, f_G. The residual variance in this case is then a function of the Greenwood frequency and described by Equation 4.7, which is restated here:

$$\sigma^2_{\text{temp}} \approx \left(\frac{f_G}{f_{BW}}\right)^{5/3}$$

The complete treatment of this term is found at the end of the previous chapter.

These variance terms can be added to give a total residual wavefront variance due to turbulence after adaptive optics correction such that [35]

$$\sigma^2 = \sigma^2_{\text{WFS}} + \sigma^2_{\text{fit}} + \sigma^2_{\text{temp}}.$$

The total residual variance is especially useful in applying the effect of adaptive optics to a model of laser propagation because it can be used to approximate the Strehl ratio with the Maréchal approximation [48]. The Maréchal approximation is

$$S(\sigma) = \frac{I_{\text{peak}}}{I_{\text{ideal}}} = e^{-\sigma^2}. \tag{5.4}$$

The Strehl ratio is the ratio of laser beam intensity on target in a non-ideal case to intensity on target in an ideal case. Notably, the contributing terms to this Strehl ratio account only for the partially corrected turbulence, not jitter. The ideal case, then, will be the resulting intensity with no turbulence or jitter. Importantly, the Maréchal approximation only holds for small residual variance, where $\sigma^2 \ll 1$ [49].

These residual phase variance terms were previously used to predict the Strehl ratios for the AO system on the La Silla 3.6 meter telescope under various atmospheric conditions [46]. These predicted Strehl ratios are listed alongside the observed Strehl ratios in Table 5.1 from a study presented by Beckers. Each column is a collection of data taken for one wavelength. The Fried parameter is proportional to $\lambda^{6/5}$, so each wavelength will correspond to a

TABLE 5.1 Strehl ratios collected from the La Silla 3.6 meter telescope adaptive optics system under various atmospheric conditions compared to the Strehl ratios predicted by the Maréchal approximation. Source: [46].

Spectral Band	Units	J	H	K	L	M
Wavelength	μm	1.2	1.68	2.23	3.87	4.75
r_0	cm	33	49	69	134	171
r_s	cm	100	100	100	100	100
V_{wind}	m/sec	5/15/25	5/15/25	5/15/25	5/15/25	5/15/25
τ_0	msec	21/7/4	31/10/6	43/14/9	84/28/17	107/36/21
f_G	Hz	6/19/32	4/13/22	3/9/15	2/5/8	1/4/6
τ_d	msec	17	17	17	17	17
f_{BW}	Hz	20	20	20	20	20
σ^2_{fit}	rad^2	2.16	1.12	0.63	0.21	0.14
σ^2_{temp}	rad^2	.15/.95/2.22	1.2/1.61/2.3	.67/.94/1.28	.22/.30/.43	.15/.20/.28
σ^2_{tot}	rad^2	2.3/3.1/4.4	1.20/1.61/2.3	.67/.94/1.28	.22/.30/.43	.15/.20/.28
$S_{\text{predicted}}$	%	10/4/1	30/20/10	51/39/28	80/74/65	86/82/76
S_{observed}	%	-	10	28	70	-

different value in the presence of the same atmosphere (constant C_n^2). The same adaptive optics system, characterized by $r_s = 100$ and $f_{BW} = 20\,\text{Hz}$, is used in each case. This data neglects the effect of signal to noise ratio in the AO system. Predicted Strehl ratios are then calculated for three different wind velocity conditions at each wavelength and compared to the observed Strehl ratio. While this study compares values in an astronomical application, the agreement between the predicted and observed Strehl ratios makes this model of the effect of AO systems a promising one for simulating AO in HELs.

5.3 Integration of Adaptive Optics into ANCHOR

The peak intensity of a laser beam after propagating a distance z is

$$I = \frac{P}{\pi a^2} e^{-\epsilon z}$$

where P is the initial laser power and ϵ is the extinction coefficient. For the ideal case, we return to the assumption of no jitter or turbulence and impose the constraint $M^2 = 1$ such that $a_{\text{ideal}} = a_d$. This gives an ideal peak intensity of

$$I_{\text{ideal}} = \frac{P}{\pi a_{\text{ideal}}^2} e^{-\epsilon z}.$$

As previously noted, the peak intensity in our non-ideal case only accounts for the case of partially corrected turbulence by adaptive optics, neglecting the effect of jitter. The Strehl ratio is then

$$S = \frac{I_{\text{peak}}}{I_{\text{ideal}}} = \frac{a_{\text{ideal}}^2}{a_{\text{ideal}}^2 + a_t^2}.$$

To solve for a_t^2, we rearrange and arrive at the expression

$$a_t^2 = \frac{a_{\text{ideal}}^2 (1 - S)}{S}. \tag{5.5}$$

This is the expression for the adaptive optics-corrected turbulence contribution to the total spot size. We use Equation 5.2 to estimate a_{ideal}^2 and Equation 5.4 to estimate the Strehl ratio. Leading to Equation 5.5, we assumed no jitter and an ideal beam. The effects of jitter and a non-ideal beam will contribute to the total spot size through the a_j^2 and a_d^2 terms in Equation 5.1.

By following this series of steps, we are able to estimate the effect of adaptive optics on target irradiance. For a clearer picture of the impact made by adaptive optics, we investigate

target irradiance in each of the two cases: the corrected case with turbulence contribution estimated by Equation 5.5 and the uncorrected case with turbulence contribution estimated by Equation 5.3. The ratio of the target irradiances from each case is the factor of performance improvement or degradation from AO contribution.

CHAPTER SIX

Simulations and Analysis

The effect of adaptive optics was simulated in four scenarios. The first scenario assumed an ideal beam $\left(M^2 = 1\right)$ and no jitter; the second accounted for reduced beam quality $\left(M^2 = 3\right)$; the third accounted for uncorrected jitter ($\theta_{\text{jitter}} = 5\,\mu\text{rad}$) — that is, the residual platform jitter after tilt correction; and the fourth scenario accounted for both effects simultaneously. For the first scenario, we simulate cases for three values for control frequency bandwidth ($f_{BW} = 10\,\text{Hz},\ 20\,\text{Hz},\ 50\,\text{Hz}$), three values for actuator spacing ($r_s = 0.015\,\text{m},\ 0.03\,\text{m},\ 0.06\,\text{m}$), and three values for beam director diameter ($D = 0.1\,\text{m},\ 0.3\,\text{m},\ 0.5\,\text{m}$). For the remaining scenarios, we look only at the uncorrected and corrected cases for one set of nominal AO parameters ($f_{BW} = 20\,\text{Hz},\ r_s = 0.3\,\text{m}$). The actuator spacing distances and control frequency bandwidths are typical values obtained from the currently available hardware [50][51]. We also assume that the signal-to-noise ratio for the wavefront sensor is sufficiently high so as not to contribute to residual error. For the astronomical application of adaptive optics, this was shown to be a plausible assumption when the reference beam is sufficiently bright [46]. The laser power is 30 kW, so the effect of thermal blooming is negligible and therefore not included in the simulations. Each irradiance plot has three contours along lines of constant peak irradiance at $100\,\text{MW/m}^2$ $\left(10\,\text{kW/cm}^2\right)$, $50\,\text{MW/m}^2$ $\left(5\,\text{kW/cm}^2\right)$, and $20\,\text{MW/m}^2$ $\left(2\,\text{kW/cm}^2\right)$. These peak irradiance values are estimated requirements for hard kills on hard, medium, and soft targets, respectively. As a metric of adaptive optics performance, we give approximate kill range increases between the tilt-compensated, or uncorrected, cases and adaptive optics compensated cases of sea-level and aerial targets. That range increase will be the distance the contour moves between the uncorrected and AO compensated cases for each set of AO configurations. Another useful metric of AO performance is in the "Improvement Factor" plots, which show the factor by which irradiance increases from the uncorrected cases to the AO compensated cases for each point in space.

The adaptive optics systems we simulate are responding to turbulence profiles generated by a program called LEEDR. The vertical C_n^2 profile that characterizes the operating environment of the following laser simulations is shown in Figure 6.1.

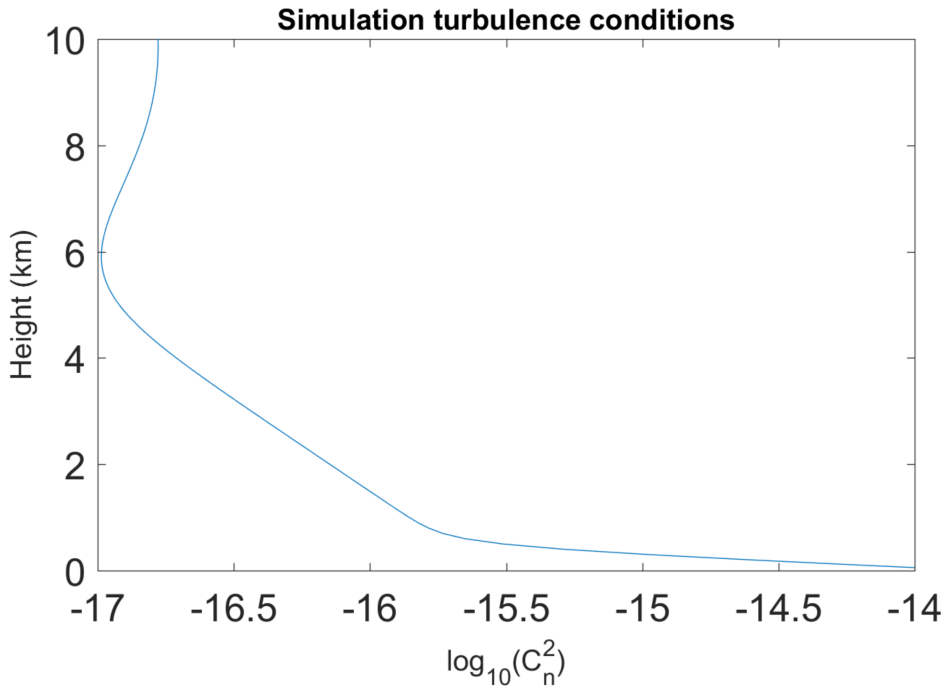

FIGURE 6.1 The typical vertical C_n^2 profile of Monterey, CA, created by LEEDR. This profile is used for the laser simulations in this chapter.

6.1 Ideal Beam Quality, No Jitter Case

The first scenario is the ideal case where we assume an perfect beam quality $\left(M^2 = 1\right)$ and no uncorrected platform jitter. For this case, we investigate the effect of control frequency bandwidth, actuator spacing, and beam director size on turbulence compensation. We study the ideal beam quality, no jitter case first to isolate the effect of AO on the turbulence contribution, a_t^2, to the total spot size in Equation 5.1. After considering this ideal case, we introduce cases with larger diffraction, a_d^2 (by increasing M^2), and jitter, a_j^2 (by increasing θ_{jitter}), contributions to identify what level of diffraction and jitter contributions begin to dominate overall spot size and reduce the benefit of using AO.

6.1.1 Effect of Increasing Control Frequency Bandwidth

To characterize the effect of control frequency bandwidth, we choose the nominal beam director size of $D = 0.3\,\text{m}$. The uncorrected case (no AO) is shown in Figure 6.2. For this beam director size, control frequencies of $f_{BW} = 10\,\text{Hz}$, $20\,\text{Hz}$, and $50\,\text{Hz}$ are evaluated and the resulting AO corrected irradiance plots are shown on the left in Figure 6.3. In the following discussion, the results for AO correction at each bandwidth frequency are compared to the uncorrected case. When $f_{BW} = 10\,\text{Hz}$, the kill range of a hard target

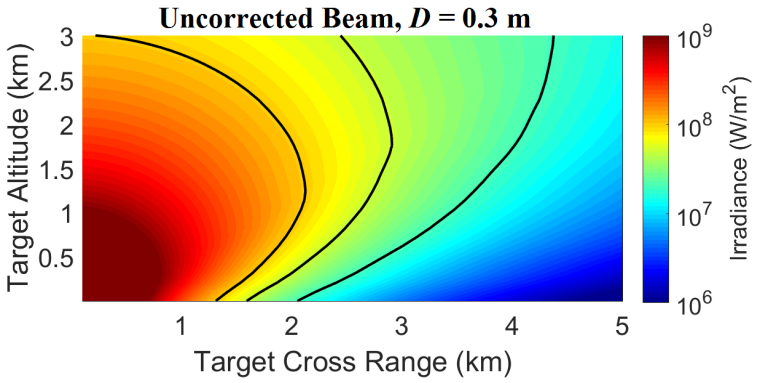

FIGURE 6.2 Uncompensated (no AO) irradiance pattern for an ideal 30 kW laser beam.

at sea-level increases by approximately 800 m and the soft target kill range increases by approximately 1 km. Increasing f_{BW} to 20 Hz can yield a range increase of 1.5 km for a hard target and 2.5 km for a soft target. For the case where $f_{BW} = 50$ Hz, the kill range for both target types approximately doubles. For aerial targets (which experience less turbulence along the path) at an altitude of 1 km, the kill range of a hard target increases by roughly 0.5 km at $f_{BW} = 10$ Hz, 1 km at $f_{BW} = 20$ Hz, and 1.5 km at $f_{BW} = 50$ Hz. For soft aerial targets, kill range increases by roughly 2 km at $f_{BW} = 10$ Hz and to ranges well beyond 5 km when $f_{BW} = 20$ Hz or 50 Hz. The target irradiance increase gained by AO compensation is also shown by the "Improvement Factor" plots that are shown next to their corresponding irradiance plots. At a range of 5 km and an altitude of 1 km, AO provides improvement factors of approximately 7 and 10 for $f_{BW} = 20$ Hz and $f_{BW} = 50$ Hz, respectively. At sea-level, those improvement factors increase to approximately 16 and 35. Interestingly, when $f_{BW} = 10$ Hz, AO does not follow the same improvement factor trend as the other two cases, where the largest improvement factors are at sea-level. For this AO system, target irradiance actually decreases from approximately 0.5 km to sea-level at a range of 5 km. We see this results because the Greenwood frequency, f_G, is greater than 10 Hz from sea-level to an altitude of 0.5 km, which means the atmosphere is changing faster than the AO can compute and apply the necessary correction. Generally, as AO control frequency bandwidth increases, irradiance on target increases.

6.1.2 Effect of Increasing Actuator Spacing

For these simulations, we assess the impact of increasing actuator spacing on laser beam performance while holding beam director diameter constant at $D = 0.3$ m. For every other set of simulations, the actuators are assumed to be in a 10×10 square grid, where the

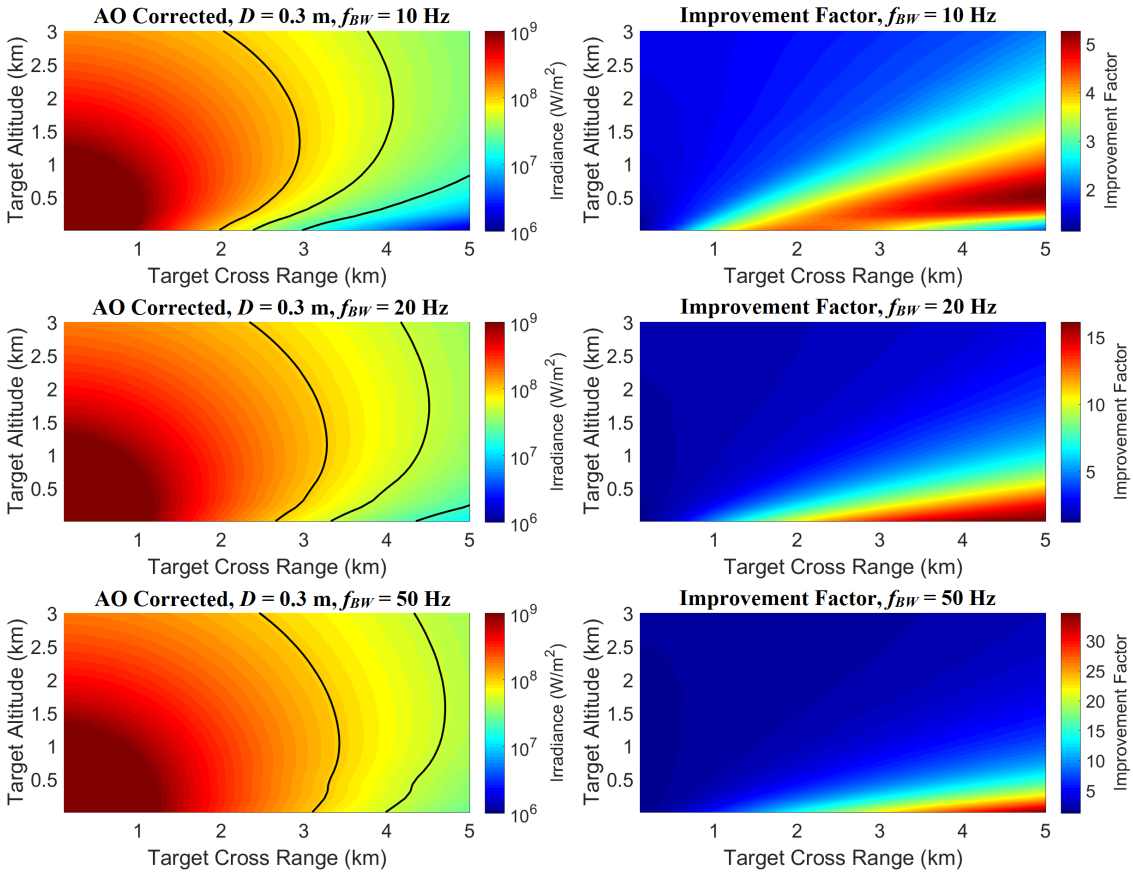

FIGURE 6.3 Peak irradiance plots of the AO corrected laser beam and corresponding "Improvement Factor" plots where the beam director diameter is held at a constant nominal value of 0.3 m and the control bandwidth varies from f_{BW} = 10 Hz to 50 Hz.

actuator spacing and beam director diameter scale proportionally such that $r_s = D/10$. In holding the beam director diameter constant for this particular set of simulations, we are evaluating actuator arrangements of 20×20, 10×10, and 5×5 square grids with corresponding actuator spacings of $r_s = 15\,\text{mm},\ 30\,\text{mm},\ 60\,\text{mm}$. The irradiance plot of the uncompensated case is shown in Figure 6.2.

The AO compensated irradiance plots are shown in Figure 6.4. For hard targets at sea level, kill range increases approximately by 1.5 km when $r_s = 15\,\text{mm}$ and when $r_s = 30\,\text{mm}$. When $r_s = 60\,\text{mm}$, the range increase is about 1 km. For soft sea level targets, the kill range increases by approximately 2.7 km, 2.4 km, and 1.5 km when $r_s = 15\,\text{mm},\ 30\,\text{mm},\ 60\,\text{mm}$, respectively. The effect of AO is less pronounced for an aerial target at an altitude of 1 km, where hard target kill ranges increase by roughly 1 km and soft target kill ranges increase to well beyond 5 km for each simulated value of actuator spacing. In any case, larger actuator separation decreases the effect of AO, but appears to have a lesser impact on system performance than does control frequency bandwidth.

6.1.3 Effect of Increasing Beam Director Diameter and Actuator Spacing

For these simulations, we increase beam director diameter size while holding the actuator arrangement constant (10×10), consequently increasing actuator spacing such that $r_s = D/10$. We hold the control frequency constant at $f_{BW} = 20\,\text{Hz}$ and simulate the cases where $D = 0.1\,\text{m},\ 0.3\,\text{m}$, and $0.5\,\text{m}$. The generated irradiance plots are shown in Figure 6.5, with uncompensated cases shown on the left and AO compensated cases shown on the right. When $D = 0.1\,\text{m}$, sea-level hard target kill range changes imperceptibly and soft target kill range increases by approximately 200 m. For convenience, we restate the case where $D = 0.3\,\text{m}$ and AO correction yields an increase of 1.5 km for hard targets and roughly 2.5 km for a soft target. The largest beam director diameter simulated, $D = 0.5\,\text{m}$, shows hard and soft target kill ranges more than doubling from uncompensated ranges of approximately 1 km and 2 km respectively. Hard aerial targets previously discussed see imperceptible kill range changes with AO when $D = 0.1\,\text{m}$, but large improvements of 1 km and 2.5 km when $D = 0.3\,\text{m}$ and $0.5\,\text{m}$, respectively. Soft aerial targets also see imperceptible kill range changes with AO when $D = 0.1\,\text{m}$, but increase well beyond 5 km for beam director diameters of size $D = 0.3\,\text{m}$ and $D = 0.5\,\text{m}$.

Notably, the irradiance patterns for the uncompensated cases change with increasing beam diameter. This phenomenon is explained by the factors that contribute to target spot

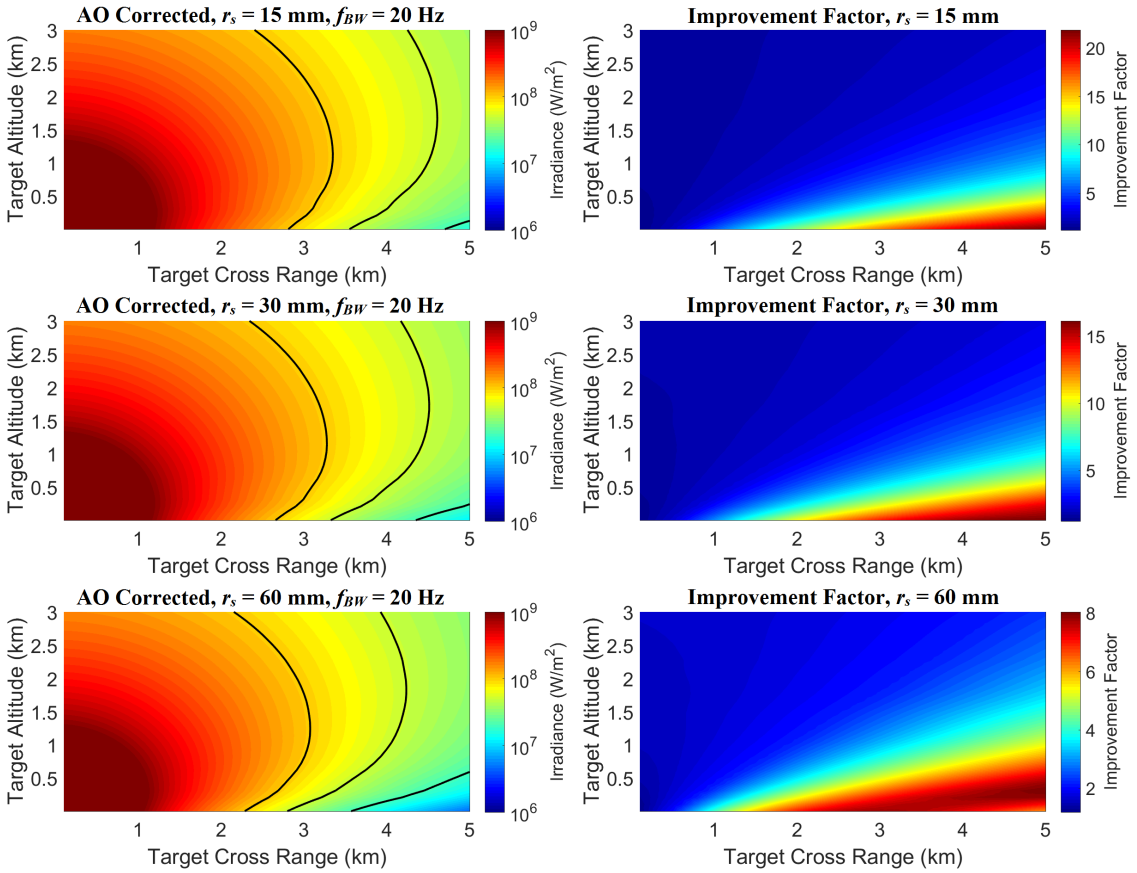

FIGURE 6.4 Irradiance plots and "Improvement Factor" plot of AO correction by increasing actuator spacing with constant beam director diameter, $D = 0.3$ m. Top: 20x20 actuators (15 mm spacing), Middle: 10x10 actuators (30 mm spacing), Bottom: 5x5 actuators (60 mm spacing)

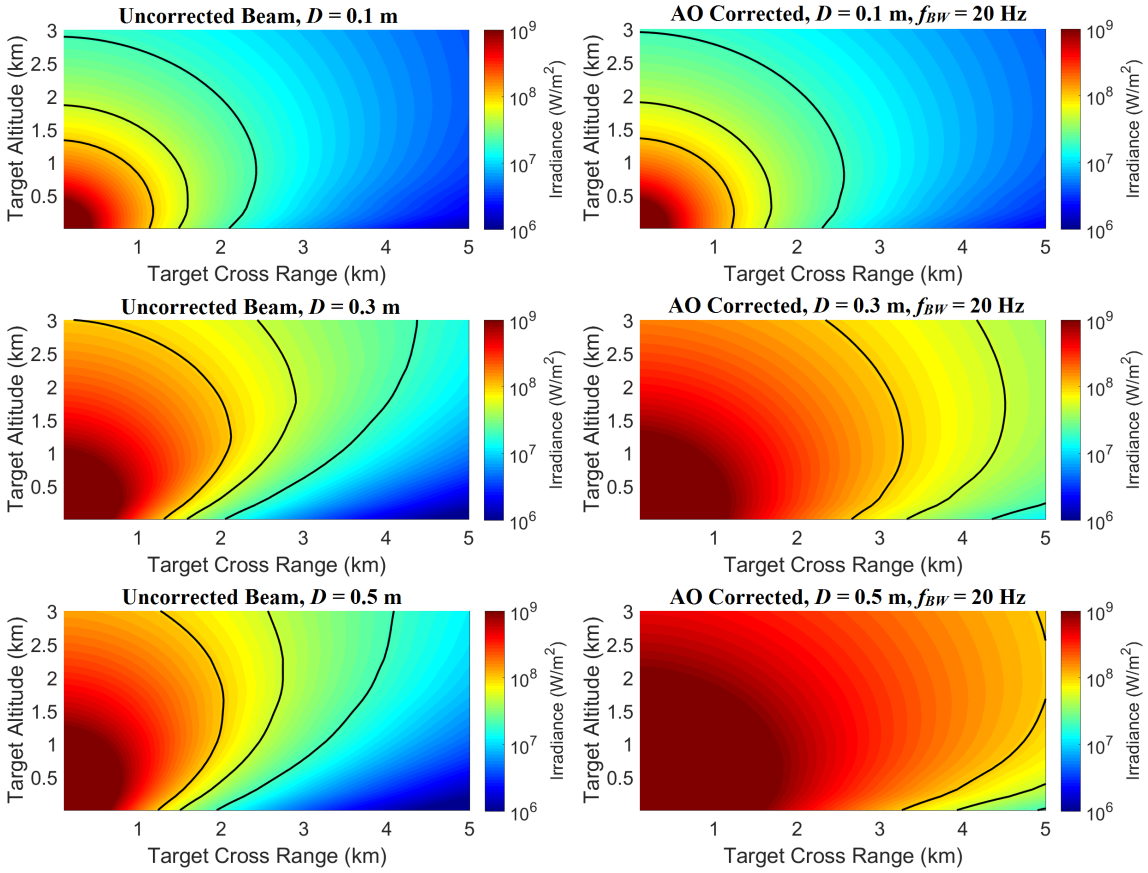

FIGURE 6.5 Peak irradiance plots of the uncorrected (left) and AO corrected (right) laser beams where the control bandwidth is held at a constant nominal value of 20 Hz and the beam director diameter increases with $D = 0.1$ m (top), $D = 0.3$ m (middle), and $D = 0.5$ m (bottom).

size, which is inversely related to irradiance. In Equation 5.1, we see that three spot size factors contribute: a_d^2, a_j^2, and a_t^2. By increasing actuator spacing r_s, and also increasing beam director diameter D, the AO is effectively decreasing a_t^2, which increases irradiance. However, increasing D also decreases the diffraction spot size a_d^2, which also increases irradiance. As such, both effects appear in the AO compensated irradiance plots (right), but only the effect of decreasing a_d^2 appears in the uncompensated irradiance plots (left). The fact that we see such little range increase with AO compensation when $D = 0.1$ m indicates that the total irradiance is dominated by diffraction, and not turbulence, meaning that mitigating turbulence with AO will yield only a small benefit for the tested conditions.

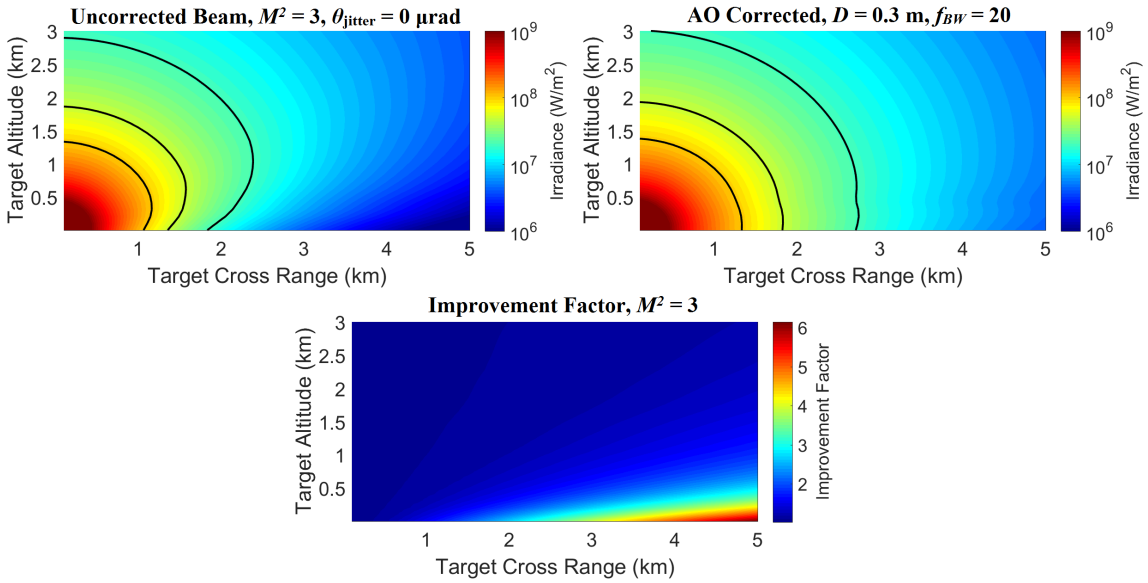

FIGURE 6.6 Peak irradiance plots for uncorrected and AO compensated laser beams where $f_{BW} = 20\,\text{Hz}$ and $D = 0.3\,\text{m}$. The laser beam source is described by $M^2 = 3$ and has no platform jitter. Additionally, the "Improvement Factor" plot shows a maximum improvement factor of approximately 6.

6.2 Non-ideal Beam Quality, No Jitter Case

For the remaining three scenarios, we will consider only the nominal cases of control loop bandwidth $f_{BW} = 20\,\text{Hz}$ and beam director size $D = 0.3\,\text{m}$. This scenario evaluates the effect of a non-ideal beam $\left(M^2 = 3\right)$ on turbulence and AO correction. By analyzing Equation 5.2, we see that increasing the value of M^2 will increase the diffraction spot size contribution to the total spot size, a_d^2, relative to the turbulence contribution, a_t^2.

As shown in Figure 6.6, a sea-level hard target kill range will increase less than 500 m from about 1 km to about 1.3 km while a soft target kill range will increase from about 1.8 km to about 2.8 km with AO correction. Aerial targets at a 1 km altitude in this environment will see kill ranges change negligibly for hard targets and increase by approximately 200 m for soft targets.

6.3 Ideal Beam Quality with Jitter Case

Our third scenario investigates the effect of uncompensated jitter $\left(\theta_{\text{jitter}} = 5\,\mu\text{rad}\right)$ on adaptive optics correction. From Figure 6.7, we can see that a hard target at sea-level can be destroyed at approximately 1 km, which increases to approximately 1.5 km with adaptive optics correction. Similarly, we can see that a soft target kill range will increase by about

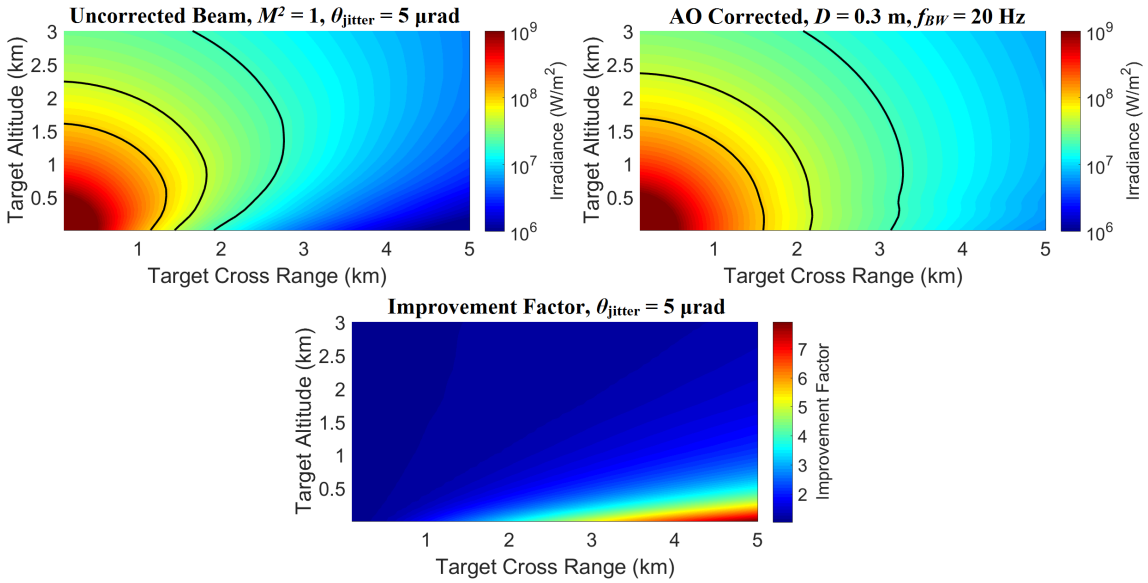

FIGURE 6.7 Peak irradiance plots for uncorrected and AO compensated laser beams where $f_{BW} = 20$ Hz and $D = 0.3$ m. The laser beam source is described by $M^2 = 1$ and has 5 μrad of uncorrected platform jitter. A maximum improvement factor is shown to be approximately 8.

1 km from approximately 2 km to 3 km. Looking again at the effect of AO on aerial target kill ranges, we see that it will increase by roughly 100 m for a hard target and 500 m for a soft target in a case with $\theta_{\text{jitter}} = 5\,\mu$rad of platform jitter.

6.4 Non-ideal Beam Quality with Jitter

This final scenario accounts for the effects of both a non-deal beam $(M^2 = 3)$ and uncompensated jitter $(\theta_{\text{jitter}} = 5\,\mu\text{rad})$ on adaptive optics correction. In this case, both a_d^2 and a_j^2 contribute to the total spot size, which will tend to mask the a_t^2 contribution and, consequently, the effect of AO on overall laser beam irradiance.

We can see that for a hard target at sea-level, AO provides a kill range increase of a approximately 100 m, and for soft targets an increased kill range of about 400 m. The kill range increases for an aerial target are approximately 200 m for hard and soft targets. The peak irradiance plots and "Improvement Factor" plot for this case are shown in Figure 6.8. Evidently, the real effects of reduced beam quality and jitter strongly influence overall beam performance, which will render AO less effective in these cases.

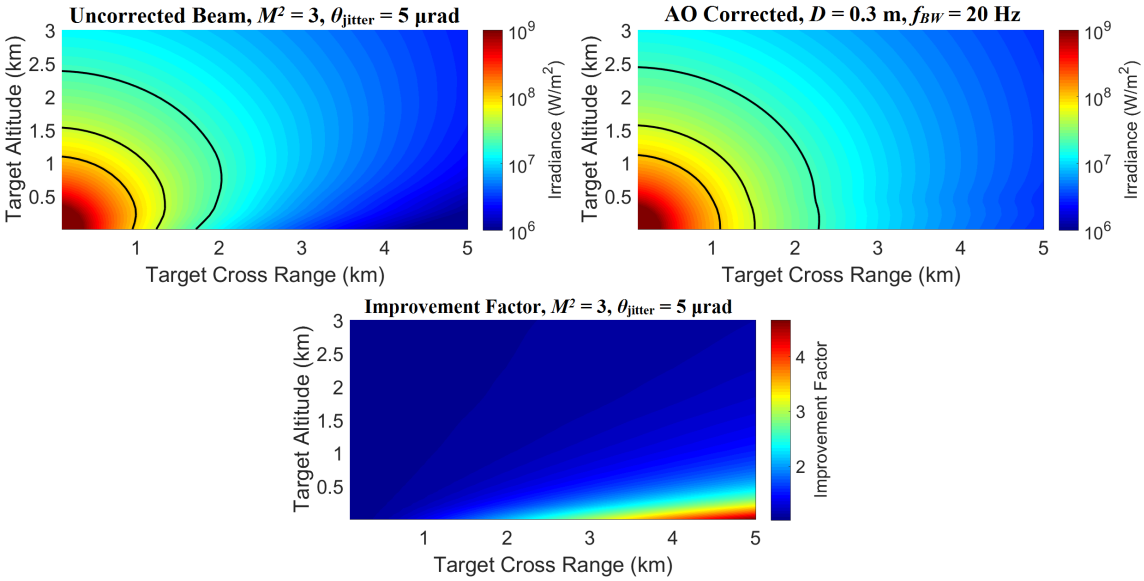

FIGURE 6.8 Peak irradiance plots for uncorrected and AO compensated laser beams where $f_{BW} = 20\,\text{Hz}$ and $D = 0.3\,\text{m}$. The laser beam source is described by $M^2 = 3$ and has $5\,\mu\text{rad}$ of uncorrected platform jitter. The maximum improvement factor is approximately 5.

CHAPTER SEVEN

Conclusions

One of the major considerations for HEL weapon use is the performance dependence on atmospheric conditions. In some cases, adaptive optics can significantly mitigate the effects of atmospheric turbulence on HEL performance. In this study, we developed a rapid method to simulate the effect of AO on target peak irradiance, enabling large parameter studies. The simple cases we examined with nominal AO system parameters show significant range improvements. Notably, the effect of adaptive optics is strongest for targets near the surface of the Earth where turbulence is stronger, represented by larger C_n^2 values from Figure 6.1.

The different scenarios that we examined illustrate the significant impact of laser beam quality and platform jitter on overall performance. In the ideal scenario, the turbulence contribution to the total spot size was relatively large, which resulted in AO correction significantly improving the kill ranges of various targets. As beam quality was reduced and platform jitter was introduced, we saw a lesser effect of AO on overall target irradiance because the turbulence contribution to the total spot size became relatively smaller. As such, it is important to understand that AO has the ability to partially correct for the diminishing effects of turbulence on laser beam performance, but the performance increase is limited to the effect of turbulence.

Future implementation of high energy laser weapons should consider the corrective capability of AO in the design process. This simulation can also inform optimization studies that vary AO system parameters and evaluate the benefit of the laser performance improvement with respect to limiting factors like cost and size of adaptive optics.

THIS PAGE INTENTIONALLY LEFT BLANK

List of References

[1] H. B. H. et al. (2013, June 24). For Sharpest Views, Scope The Sky With Quick-Change Mirrors. [Online]. Available: http://www.npr.org/2013/06/24/190986008/for-sharpest-views-scope-the-sky-with-quick-change-mirrors

[2] M. Olson, "History of laser weapon research," Defence Technical Information Center, Dahlgren, VA, Tech. Rep. ADA557756, 2012.

[3] Slab Lasers. (n.d.). RP Photonics. [Online]. Available: https://www.rp-photonics.com/slab_lasers.html

[4] J. Blau, "Introduction to free electron lasers," lecture slides from Electric Ship Weapon Systems, Dept. of Physics, Naval Postgraduate School, Monterey, CA, Fall 2016.

[5] J. L. Burley, "Comparison of high energy laser expected dwell times and probability of kill for mission planning scenarios in actual and standard atmospheres," Master's thesis, Air Force Institute of Technology, 2012.

[6] J. Blau, "Directed energy weapons: History," lecture slides from Electric Ship Weapon Systems, Dept. of Physics, Naval Postgraduate School, Monterey, CA, Fall 2016.

[7] High Energy Laser Systems Test Facility. (n.d.). White Sands Missile Range. [Online]. Available: http://www.wsmr.army.mil/testcenter/testing/landf/Pages/HighEnergyLaserSystemsTestFacility.aspx

[8] The Strategic Defense Initiative (SDI): Star Wars. (n.d.). The Cold War Museum. [Online]. Available: http://www.coldwar.org/articles/80s/SDI-StarWars.asp

[9] Missile Defense Umbrella? (2011, Jan. 11). Center for Strategic and International Studies. [Online]. Available: https://web.archive.org/web/20110111093235/http://csis.org/blog/missile-defense-umbrella

[10] C. Kopp, "High energy laser directed energy weapons," Air Power Australia, Melbourne, Australia, Tech. Rep. APA-TR-2008-0501, 2014.

[11] J. Tierney. (2008, Nov. 21). Sci-Fi Ray Gun Debuts in Iraq. *The New York Times*. [Online]. Available: https://tierneylab.blogs.nytimes.com/2008/11/21/sci-fi-ray-gun-debuts-in-iraq/comment-page-6/?mcubz=1&_r=0

[12] B. Chappell. (2014, Dec. 10). Watch: Navy Ship Uses Energy Weapon In Persian Gulf. NPR. [Online]. Available: http://www.npr.org/sections/thetwo-way/2014/12/10/369922915/watch-navy-ship-uses-energy-weapon-in-arabian-gulf

[13] P. E. Nielsen, *Effects of Directed Energy Weapons*. Albuquerque, NM: DEPS, 2009.

[14] J. R. Cook, "Atmospheric propagation of high energy lasers and applications," *American Institute of Physics*, vol. 766, no. 58, 2005.

[15] G. P. P. et al., *Introduction to laser weapon systems*, J. S. Accetta and B. A. Kohl, Eds. Albuquerque, NM: Directed Energy Professional Society, 2010.

[16] F. G. Gebhardt, "High power laser propagation," *Applied Optics*, vol. 15, no. 6, pp. 1479–1493, 1976.

[17] H. Weichel, *Laser beam propagation in the atmosphere*, R. F. Potter, Ed. The International Society for Optical Engineering, 1990.

[18] J. D. Schmidt, *Numerical Simulation of Optical Methods*. SPIE, 2010.

[19] L. C. A. et al., "Near-ground vertical profile of refractive-index fluctuations," *Proceedings of SPIE*, vol. 7324, April 2009.

[20] D. L. Fried, "Statistics of a geometric representation of wavefront distortion," *Journal of the Optical Society of America*, vol. 55, no. 11, pp. 1427–1435, 1965.

[21] R. K. Tyson, *Introduction to Adaptive Optics*. SPIE, 2000.

[22] D. P. Greenwood, "Bandwidth specification for adaptive optics systems," *Journal of the Optical Society of America*, vol. 67, no. 3, pp. 390–393, 1977.

[23] K. Cohn and J. Blau, "Atmospheric propagation," lecture slides from Electric Ship Weapon Systems, Dept. of Physics, Naval Postgraduate School, Monterey, CA, Fall 2016.

[24] H. B. et al., "Algebraic model for cw thermal-blooming effects," *Applied Optics*, vol. 18, no. 15, pp. 2638–2644, 1979.

[25] F. L. Pedrotti and L. S. Pedrotti, *Introduction to Optics,* 2nd ed. R. Henderson, Ed. Prentice-Hall, Inc., 1993.

[26] M. Born and E. Wolf, *Principles of optics,* 7th ed. Cambridge University Press, 1999.

[27] R. J. Noll, "Zernike polynomials and atmospheric turbulence," *Journal of the Optical Society of America*, vol. 66, no. 3, pp. 207–211, 1976.

[28] J. Y. Wang and D. E. Silva, "Wave-front interpretation with zernike polynomials," *Journal of the Optical Society of America*, vol. 19, no. 9, pp. 1510–1518, 1980.

[29] Pyramid of Zernike polynomials. (n.d.). *Wikipedia.* [Online]. Available: https://en.wikipedia.org/wiki/User:Zom-B#/media/File:Zernike_polynomials2.png

[30] S. Gibson, "Atmospheric propagation of high energy lasers: Modeling, simulation, tracking, and control," University of California, Los Angeles, Tech. Rep., 2008.

[31] B. C. . Platt and R. Shack, "History and principles of shack-hartmann wavefront sensing," *Journal of Refractive Surgery*, vol. 17, pp. S573–S577, Sept./Oct. 2001.

[32] F. Roddier, "Curvature sensing and compensation: a new concept in adaptive optics," *Journal of the Optical Society of America*, vol. 27, no. 7, pp. 1223–1225, 1988.

[33] Shack-Hartmann Wavefront Sensors. (n.d.). Thorlabs. [Online]. Available: https://www.thorlabs.com/catalogpages/V21/1613.PDF

[34] R. A. et al., *Topics in Adaptive Optics*, R. K. Tyson, Ed. Rijeka, Croatia: InTech, 2012.

[35] R. K. Tyson, *Principles of Adaptive Optics,* 2nd ed. Cambridge, MA: Academic Press, 1998.

[36] J. W. Hardy and A. J. MacGovern, "Shearing interferometry: A flexible technique for wavefront measurement," *Proceedings of SPIE*, vol. 0816, no. 180, March 1987.

[37] Shearing Interferometers. (n.d.). Thorlabs. [Online]. Available: https://www.thorlabs.com/newgrouppage9.cfm?objectgroup_id=2970

[38] N. D. et al., "Requirements for discrete actuator and segmented wavefront correctors for aberration compensation in two large populations of human eyes," *Journal of the Optical Society of America*, vol. 46, no. 20, pp. 4501–4514, July 2007.

[39] K. N. et al., "Transformation of a laser beam intensity profile by a deformable mirror," *Journal of the Optical Society of America*, vol. 21, no. 3, pp. 168–170, Feb. 1996.

[40] I. K. et al., "Development of deformable mirror composed of piezoelectric thin films for adaptive optics," *IEEE Journal of Selected Topics in Quantum Electronics*, vol. 13, no. 2, pp. 155–161, Mar./Apr. 2007.

[41] L. H. et al., "Modified gaussian influence function of deformable mirror actuators," *Journal of the Optical Society of America*, vol. 16, no. 1, pp. 108–114, Jan. 2008.

[42] C. R. et al., "Mounting with compliant cylinders for deformable mirrors," *Journal of the Optical Society of America*, vol. 40, no. 7, pp. 1536–1539, 2015.

[43] J. C. D. et al., "Low-order adaptive deformable mirror," *Journal of the Optical Society of America*, vol. 37, no. 21, pp. 4663–4668, 1998.

[44] X.-H. X. et al., "Design, fabrication and characterization of a bulk-pzt-actuated mems deformable mirror," *Journal of Micromechanics and Mircroengineering*, vol. 17, no. 12, p. 2439, Oct. 2007.

[45] Introduction: Frequency Domain Methods for Controller Design. (n.d.). [Online]. Available: http://ctms.engin.umich.edu/CTMS/index.php?example=Introduction&section=ControlFrequency. Control Tutorials for MATLAB & SIMULINK.

[46] J. M. Beckers, "Adaptive optics for astronomy: Principles, performance, and applications," *Annual Review of Astronomy and Astrophysics*, vol. 31, pp. 13–62, 1993.

[47] J. W. Hardy, "Instrumental limitations in adaptive optics for astronomy," *Proceedings of SPIE*, vol. 1114, no. 2, Sept. 1989.

[48] T. S. Ross, "Limitations and applicability of the marechal approximation," *Journal of the Optical Society of America*, vol. 48, no. 10, pp. 1812–1818, 2009.

[49] G. V. et al., *Oko Guide to Adaptive Optics,* 4th ed. Flexible Optical BV, Rijswijk, Netherlands, 2013.

[50] Aokit bio: Build your ideal adaptive optics system for microscopy. (n.d.). Imagine Optic. [Online]. Available: http://www.imagine-optic.com/en/product/aokit-bio/0/0/

[51] Shack-Hartmann wavefront sensors, 1.3 Megapixel Resolution. (n.d.). Thorlabs. [Online]. Available: https://www.thorlabs.com /newgrouppage9.cfm?objectgroup_id=2946

Initial Distribution List

1. Defense Technical Information Center
   Ft. Belvoir, Virginia

2. Dudley Knox Library
   Naval Postgraduate School
   Monterey, California